



# Water Mass and Biogeochemical Variability in the Kerguelen Sector of the Southern Ocean: A Machine Learning Approach for a Mixing Hot Spot

Isabella Rosso<sup>1</sup> , Matthew R. Mazloff<sup>1</sup> , Lynne D. Talley<sup>1</sup> , Sarah G. Purkey<sup>1</sup> , Natalie M. Freeman<sup>1</sup> , and Guillaume Maze<sup>2</sup>

<sup>1</sup>Scripps Institution of Oceanography, University of California, San Diego, La Jolla, CA, USA, <sup>2</sup>Ifremer, University of Brest, CNRS, IRD, Laboratoire d'Océanographie Physique et Spatiale, IUEM, 29280, Plouzané, France

## Key Points:

- An unsupervised classification technique, applied to temperature and salinity float data, is used to sort the profiles into frontal zones
- In eddy fields the variability of physical and biogeochemical properties is more than twice as large as the mean zonal variability
- The intense eddy variability drives lateral physical processes that cause the large property variance

## Supporting Information:

- Supporting Information S1

## Correspondence to:

I. Rosso,  
irosso@ucsd.edu

## Citation:

Rosso, I., Mazloff, M. R., Talley, L. D., Purkey, S. G., Freeman, N. M., & Maze, G. (2020). Water mass and biogeochemical variability in the Kerguelen sector of the Southern Ocean: A machine learning approach for a mixing hot spot. *Journal of Geophysical Research: Oceans*, 125, e2019JC015877. <https://doi.org/10.1029/2019JC015877>

Received 15 NOV 2019

Accepted 2 MAR 2020

Accepted article online 10 MAR 2020

**Abstract** The Southern Ocean (SO) is one of the most energetic regions in the world, where strong air-sea fluxes, oceanic instabilities, and flow-topography interactions yield complex dynamics. The Kerguelen Plateau (KP) region in the Indian sector of the SO is a hot spot for these energetic dynamics, which result in large spatiotemporal variability of physical and biogeochemical properties throughout the water column. Data from Argo floats (including biogeochemical) are used to investigate the spatial variability of intermediate and deep water physical and biogeochemical properties. An unsupervised machine learning classification approach is used to organize the float profiles into five SO frontal zones based on their temperature and salinity structure between 300 and 900 m, revealing not only the location of frontal zones and their boundaries but also the variability of water mass properties relative to the zonal mean state. We find that the variability is property dependent and can be more than twice as large as the mean zonal variability in intense eddy fields. In particular, we observe this intense variability in the intermediate and deep waters of the Subtropical Zone; in the Subantarctic Zone just west of and at KP; east of KP in the Polar Frontal Zone, associated with intense eddy variability that enhances deep waters convergence and mixing; and, as the deep waters upwell to the upper 500 m and mix with the surface waters in the southernmost regimes, each property shows a large variability.

**Plain Language Summary** The Southern Ocean strongly influences the global climate system, by absorbing, storing, and redistributing heat and carbon across the different ocean basins. Thanks to an increasing number of observations from autonomous instruments, called Argo floats, our understanding of this harsh environment has deepened in the last two decades. Here we use a machine learning technique to automatically classify the float measurements and sort them in regimes with similar properties based on their temperature and salinity vertical structure. The classification results are consistent with previous studies but are here used to reveal regions where mixing between different types of waters is likely to be occurring. By sorting the float profiles into regimes, we can diagnose regions with larger variation of properties and highlight the transition of the properties across regimes. Given the increasing volume of observations that instruments like the Argo floats are building, a method such as the technique implemented in this study represents a valuable tool that can help to automatically reveal similarities in dynamical regimes.

## 1. Introduction

The Kerguelen Plateau (KP) is a prominent shallow topographic barrier to the Antarctic Circumpolar Current (ACC) in the Indian sector of the Southern Ocean, spanning 2,000 km of latitude and reaching 3,000 m in depth. The surface, intermediate, deep, and abyssal circulation around the plateau is complex and acts to mix waters from different sources (e.g., Aoki et al., 2008; Llort et al., 2018; Park & Gamberoni, 1997; Tamsitt et al., 2017), enhance phytoplankton productivity (e.g., Maraldi et al., 2009; Park, Roquet, et al., 2008; Van Beek et al., 2008), and connect Antarctic-sourced bottom waters with the lower latitudes (Donohue et al., 1999; Fukamachi et al., 2010), with implications for carbon and heat budgets (Tamsitt et al., 2016; Rosso et al., 2017). Upon interaction with the plateau, the ACC is deflected, with most of the transport

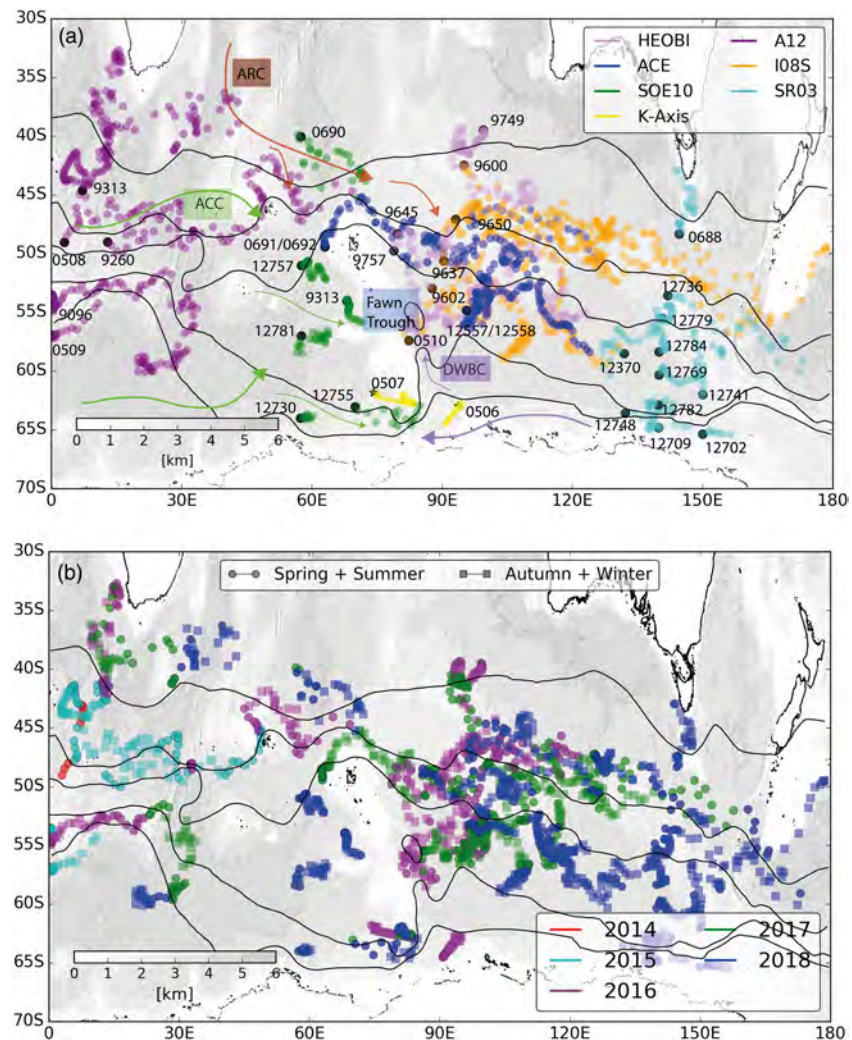


**Figure 1.** Trajectories of the biogeochemical-Argo floats from the Southern Ocean Carbon and Climate Observations and Modeling project in the Indian sector of the Southern Ocean (September 2018 snapshot), colored by (a) their deployment cruise (Table S1) and (b) profile year (markers indicate sample season: warmer austral spring and summer months [circles] and colder austral autumn and winter months [squares]). The Orsi et al. (1995) fronts (black contours), from south to north, the southern boundary of the ACC, Southern Antarctic Circumpolar Current Front, Polar Front, Subantarctic Front, and Subtropical Front, are overlain on bathymetry (grayscale map; ETOPO1 Amante & Eakins, 2009). Trajectories of southernmost floats sampling under sea ice are estimated using linear interpolation (appear as near-straight pathways; e.g., Float #12702). Major currents in (a) are labeled, with flow direction indicated by arrows: Agulhas Return Current (ARC), Antarctic Circumpolar Current (ACC), and Deep Western Boundary Current (DWBC). The Fawn Trough is also indicated.

occurring north of the plateau (Park et al., 1993) and through the Fawn Trough (McCartney & Donohue, 2007; Park & Gamberoni, 1997; Park, Roquet, et al., 2008) that divides KP into northern and southern parts (Figure 1a). However, much of these complex dynamics are still poorly understood.

In recent decades, core (i.e., temperature and salinity only data) and biogeochemical-Argo (BGC-Argo) profiling floats have greatly augmented the spatial and temporal coverage of the top 2,000 m of the Southern Ocean, a region that, because of the extreme conditions, is only marginally observed by ship-based platforms. In the present study, we use a set of core and BGC-Argo floats (the latter as part of the Southern Ocean Carbon and Climate Observations and Modeling [SOCCOM] project) to explore the variability of physical and BGC parameters (section 4) within the intermediate and deep waters of the south Indian Ocean, in relation to Southern Ocean regimes and to the area around KP.

In order to classify individual Argo and BGC-Argo profiles into unique Southern Ocean regimes, we use a Profile Classification Model (PCM) approach based on machine learning unsupervised classification

techniques (Maze, Mercier, & Cabanes, 2017). The PCM is applied to individual temperature and salinity profiles, which are organized into groups with similar properties. This approach has shown skills in systematically classifying vertical profiles of the North Atlantic (Maze, Mercier, Fablet, et al., 2017) and Southern Oceans (Jones et al., 2018), without relying on user-specified ad hoc criteria for each profile. The PCM automatically identifies multiple Southern Ocean zones, the Agulhas Current, Subtropical and Subantarctic Mode Water (SAMW) formation regions, and the system of currents around Australia.

A short review of the circulation, dynamics, and water masses examined in this study is presented in section 2. The data set is presented in section 3. We introduce the use of the PCM technique to classify float profiles in section 4 and present the resulting Southern Ocean frontal zones in section 5.1. We then highlight the variability of the physical and BGC properties of the Antarctic Intermediate Water (AAIW) and Upper Circumpolar Deep Water (UCDW) across the different regimes depicted by the PCM classification and in relation to topographic features (sections 5.3 and 5.4, respectively). Section 6 is a discussion with final remarks.

## 2. Background

In this section we describe some of the fundamental features of the South Indian Ocean circulation and dynamics and highlight key questions for this study.

As the ACC encounters KP, its transport is divided into three different pathways, each with intensified, narrow currents guided by topography. The portion of the ACC that flows north of KP interacts with the southern limb of the South Indian subtropical gyre, which reaches the plateau via the Agulhas Return Current (Park et al., 1993). The Agulhas Return Current enters from the Crozet Basin, just west of KP (Park et al., 1993), carrying salty and warm waters to the fresher and colder waters of the ACC. Here, eddy-induced transport convergence and subduction at both the mode and intermediate classes occurs (Sallée et al., 2010). A narrow and deep passage, the Fawn Trough (sill depth: 2,650 m), divides KP around 56°S, 78°E and channels Antarctic waters into a strong, northeastward flowing current (Fawn Trough Current) toward the Australian-Antarctic Basin (east of KP) (e.g., Park et al., 2009, 2014; Roquet et al., 2009).

Just south of KP, the eastward flow of the ACC navigates a narrow opening through the Princess Elizabeth Trough (PET; as deep as ~3,700 m at 64°S). In the southern part of PET, the westward flow of the Antarctic Slope Front carries waters from the Australian-Antarctic basin (Aoki et al., 2008; Donohue et al., 1999). These flows in the PET mingle the waters from both the Weddell Basin and the Adélie coast, turn northward around KP, and form a northward deep western boundary current that hugs the eastern edge of the southern plateau (e.g., Aoki et al., 2008; Donohue et al., 1999; Fukamachi et al., 2010). Can float-based temperature and salinity profiles be used by the PCM to automatically identify these pathways?

Downstream (east) of KP, the surface, deep, and bottom waters all converge into a system of highly energetic mesoscale and submesoscale eddies and fronts (e.g., Llort et al., 2018; Rosso et al., 2014), which can facilitate the exchange of different water masses by injection and intrusion mechanisms (Llort et al., 2018). Their pathways, then, continue northward across the mean flow, modified by mixing with ACC waters. Frontal positions are complex and highly variable in space and intensity (Freeman et al., 2016; Sokolov & Rintoul, 2009a), especially upstream and downstream of topographic features that play a major role in controlling their position. Specifically, near and at Crozet Plateau and KP, the Subtropical Front (STF), Polar Front (PF), and Subantarctic Front (SAF) can merge and divide into multiple branches (Freeman et al., 2016; Park, Fuda, et al., 2008; Sokolov & Rintoul, 2009b). Facilitated by strong cross-frontal injections and high eddy kinetic energy downstream of major topographic features, saltier subtropical waters exchange with subantarctic waters in Crozet Basin and pulses of AAIW are injected into the Subtropical Zone (STZ) (Park & Gamberoni, 1997). In addition, enhanced vertical velocities associated with increased mesoscale and submesoscale energy downstream of topography can trigger subduction events from the surface to the mixed layer. These subduction events can facilitate the (1) export of carbon below the mixed layer (Llort et al., 2018) or (2) flux of dissolved inorganic iron into the surface waters and are fundamental in triggering enhanced phytoplankton productivity in this region (Rosso et al., 2016). Can the PCM be used to identify frontal positions? How do injection events impact the classification of a float profile?

High mesoscale energy downstream of the plateau favors not only the vertical flux of iron (Park et al., 2014; Rosso et al., 2014) but also the upwelling of carbon and macronutrient rich deep water masses to the surface

(Tamsitt et al., 2017). Localized upwelling into the mixed layer also occurs at the mode and intermediate water classes near KP (Sallée et al., 2010). Here, turbulent diapycnal mixing is enhanced throughout the full water column, driven by processes associated with local wind and tides (near-surface), internal wave shear and strain variance (interior), or generated by geostrophic flow over rough topography (near-bottom Meyer et al., 2015; Whalen et al., 2015). Meyer et al. (2015) found that diapycnal mixing is particularly enhanced in this ACC frontal region, driven by the dissipation of internal waves generated by the ACC's interaction with KP. This mixing is particularly important at the boundary between the AAIW and the denser UCDW, which drives water mass transformation and consequently contributes to the overturning circulation (Meyer et al., 2015). Are there areas of major mixing that can be identified by the PCM classification method?

Following Orsi et al. (1995), the Southern Ocean regimes can be classified into the following zones, from north to south: STZ (north of the STF), Subantarctic Zone (SAZ; between the STF and SAF), Polar Frontal Zone (PFZ; between the SAF and PF), and Antarctic-Southern Zone (ASZ; south of the PF and north of the southern boundary of the ACC, and including both of Orsi et al.'s Antarctic and Southern Zones). In this study, we focus on the spatial variability of the intermediate and deep water masses in the Indian sector of the Southern Ocean in relation to KP and these Southern Ocean frontal zones, which are in fact uniquely represented using the PCM technique applied here. AAIW represents one of the major water masses originating in the Southern Ocean and allows for the ventilation and transport of surface signals through much of the world's oceans (Talley, 1996). AAIW is a cold and low-salinity water mass, defined by a salinity minimum at an intermediate depth of ~600–1,000 m in the waters north of the SAF (McCartney, 1977; Orsi et al., 1995; Talley, 2013), forming in the SAZ from the sinking waters south of the SAF at specific sites, such as the southeast Pacific (e.g., McCartney, 1977; Sloyan et al., 2010) and the southwest Atlantic Ocean (e.g., Piola & Gordon, 1989). AAIW is modified by mixing and intrusion of waters with different source origins throughout the Southern Ocean, such as in the southeast Pacific, southwest Atlantic (e.g., McCartney, 1977; Piola & Georgi, 1982), or central south Indian Ocean (e.g., Park & Gamberoni, 1997). As a water mass sourced from surface waters, AAIW oxygen content is relatively high but varies spatially across the Southern Ocean due to localization of its source and subsequent modification (e.g., Talley, 1996). In the south Indian Ocean, the AAIW's core sits at an isopycnal with potential density  $\Sigma_0 \sim 27.3 \text{ kg/m}^3$  (Talley et al., 2011) and with oxygen concentration as high as  $\sim 270 \text{ } \mu\text{mol/kg}$  (Park & Gamberoni, 1997). Where are the regions of larger variability associated with the different physical and BGC properties? Can these regions be described by a single property, or are they property dependent?

Above AAIW and north of the SAF, at a potential density of  $\Sigma_0 \sim 26.8 \text{ kg/m}^3$ , lies SAMW (e.g., Aoki et al., 2007; Hanawa & Talley, 2001; McCartney, 1977; Sloyan & Rintoul, 2001). This thick homogeneous layer ventilates the thermocline and originates from a combination of different processes, such as air-sea exchange, deep wintertime mixed layers, diapycnal mixing, advection, and eddy mixing (Cerovečki & Mazloff, 2016; Hanawa & Talley, 2001; Sallée et al., 2006; Sloyan et al., 2010) and is characterized by a minimum in potential vorticity (PV) (Hanawa & Talley, 2001). The southeast Indian Ocean east of KP is a major source of SAMW (McCarthy & Talley, 1999), with a pool of low PV centered around  $90^\circ\text{E}$ ,  $40^\circ\text{S}$  and extending toward Australia. Here, the region's unique bathymetry controls the location of fronts (e.g., Sallée et al., 2006; Sokolov & Rintoul, 2009b) and SAMW formation (located at the divergence of the STF and SAF Sallée et al., 2006), as well as the flavors of different types of SAMW. Both AAIW and SAMW play a fundamental role in regulating fluxes, storage, and transport of carbon, freshwater, heat, and nutrients (Ito et al., 2010; Sabine et al., 2004; Sarmiento et al., 2004) and thus play a major role in controlling Earth's climate. Based on temperature and salinity profiles only, can the PCM classification method identify the south Indian Ocean SAMW region?

Below AAIW lies UCDW, which can be identified by its core at  $\Sigma_0 \sim 27.6 \text{ kg/m}^3$  (Talley et al., 2011). UCDW is a large volume of water, which originates from the deep waters of the Pacific and Indian Oceans, with modifications in the Southern Ocean (Talley et al., 2011). As an old water mass, UCDW is characterized by an oxygen minimum and high nutrient content. In the southernmost zones of the Southern Ocean (i.e., south of the PF), upwelling UCDW brings very old and nutrient-rich waters to the surface, stimulating carbon outgassing (e.g., Gray et al., 2018; Gruber et al., 2009; Takahashi et al., 2009) and local (Prézelin et al., 2000) and remote biological productivity (Sarmiento et al., 2004). BGC profiling floats have recently been used to identify a much stronger outgassing of natural carbon in these regions than previously understood (Gray et al., 2018). Where are the regions of major variability associated with the different properties in the UCDW, and can these regions be described by a single property, or are they property dependent?

### 3. Data: Autonomous Profiling Floats

The present study is focused on variability of physical and BGC properties in the Indian sector of the Southern Ocean, using core Argo floats that measure temperature and salinity, and BGC-Argo floats that additionally measure oxygen ( $O_2$ ), nitrate ( $NO_3^-$ ), and pH. Our focus is on Southern Ocean regimes upstream and downstream of KP.

Core and BGC-Argo profilers drift freely at 1,000 m, descend to 2,000 m after  $\sim 10$  days and ascend to the surface, profiling the water column. At the surface, they transmit the measurements via satellite. In this work, we use only core and BGC-Argo float data with quality control equal to 1, 5, or 8 (i.e., flagged as “good,” “value changed,” or “estimated value,” respectively, as per Table 2 of the Argo manual, Argo Data Management Team, 2017; Johnson et al., 2017; Wong et al., 2012). Argo float vertical sampling varies across float and sensor types (see Table 16 in Argo Data Management Team, 2017, for a description). The vertical resolution of BGC-Argo data is higher in the upper 100 m and decreases with increasing depth (Johnson et al., 2017). We therefore linearly interpolate each Argo and BGC-Argo vertical profile onto regular 1-dbar vertical spacing. The accuracy of oxygen data is  $1 \pm 1\%$ , nitrate is  $0.5 \pm 0.5 \mu\text{mol/kg}$ , and pH is  $0.005 \pm 0.007$  (Johnson et al., 2017). For more technical details about BGC sensors, see Johnson et al. (2017) and Riser et al. (2018).

This study uses Argo and BGC-Argo profiles south of  $30^\circ\text{S}$  and between  $0^\circ$  and  $180^\circ\text{E}$ . The quality-controlled September 2018 Argo snapshot was extracted from the Global Data Assembly Center (Argo Data Management Team, 2018); 822 Argo floats were selected in the area of study between December 2010 and September 2018, with a total of 103,718 profiles, not including the BGC-Argo profiles. The quality-controlled SOCCOM September 2018 snapshot used in this study can be found in Johnson et al. (2018). Between December 2014 and September 2018, 36 BGC-Argo profiling floats (with more than five profiles) were present in the study area (Table S1 in the supporting information and Figure 1), for a total of 1,847 profiles. The SOCCOM floats, mostly fabricated at the University of Washington from components purchased from Teledyne/Webb Research (Apex floats), but with some BGC Navis floats purchased from SeaBird Electronics, are listed in Table S1. They were deployed during the course of several U.S. and international oceanographic campaigns (Table S1): three GO-SHIP (A12, I08S, and SR03; <https://usgoship.ucsd.edu>) and four non GO-SHIP cruises (IN2016\_V01, AU1603, SOE10, and ACE).

## 4. Method

### 4.1. Classification of Profiles Into Regimes Using Machine Learning

The waters in the Southern Ocean are often classified into zones divided by property fronts (e.g., temperature, salinity, nitrate, and oxygen) (Gray et al., 2018; Orsi et al., 1995): the STZ, with the warmest and most saline waters; the SAZ, with cooler and fresher waters relative to the STZ; the PFZ, with a characteristic subsurface temperature minimum that tracks the Antarctic surface water; the ASZ within the southern ACC, which is characterized by carbon- and nutrient-rich waters shoaling toward the surface; and the Sea Ice Zone (SIZ), which includes waters covered with sea ice during colder months. Because these fronts meander in space and time (Freeman et al., 2016; Sokolov & Rintoul, 2009a), investigating changes of water properties within each regime can be complicated. A straightforward but limited approach is to separate float profiles according to the mean position of fronts (e.g., as in Gray et al., 2018). A more data-intensive approach, which takes frontal meandering into account, is to classify each profile based on specified characteristics of each frontal zone using Orsi et al. (1995) for the zone definitions (e.g., as in Williams et al., 2018).

Here we use an unsupervised machine learning approach that groups profiles with similar vertical distributions of properties (Maze, Mercier, & Cabanes, 2017, called this a PCM). If the historical choices of frontal zone properties are reasonable, then the machine learning approach should result in groupings that closely resemble the frontal zone groupings, and in fact this is what we find. In this method, the time-variable position of the fronts, or regimes, naturally arises from the spatial distribution of the groups defined by the data, and the statistics of the groups can account for the variability of front meanders. Given the large number and sparse coverage of profiles, the use of a PCM is particularly suited to investigating the variability of water properties in relation to the presence of the KP and Southern Ocean regimes.

A PCM determines, without supervision, categories for a collection of ocean profiles. For each individual profile, the model gives the probability that it belongs to one of the determined categories. Our PCM

methodology is based on Maze, Mercier, Fablet, et al. (2017), where the authors successfully used Argo temperature profiles in the North Atlantic Ocean to characterize the different regimes in the region. The PCM method was applied recently to Southern Ocean Argo floats by Jones et al. (2018), who classified the profiles into the major current systems and regimes using temperature data alone. In the present work, we significantly extend the PCM procedure using both temperature and salinity data, an implementation that gives a more robust identification of Southern Ocean zones, which are commonly defined by both temperature and salinity (Orsi et al., 1995). The advantage of using this unsupervised technique is that it treats the numerous profiles systematically, without relying on ad hoc criteria for each profile, which can change over time (Jones et al., 2018). The method identifies the different regimes, allowing one to then diagnose hot spots of larger property variability within the identified regime. Frontal locations become apparent as connected quasi-zonal bands of variability arising from frontal meandering.

#### 4.2. The PCA Methodology

The PCM requires float data preparation and a classifier algorithm. For the classifier algorithm we chose a Gaussian Mixture Model (Bilmes et al., 1998; Bishop, 2006). This algorithm is based on the assumption that the data are generated by a mixture of a number of Gaussian distributions in  $D$  dimensions (defined by the number of principal components, as explained below) and takes into account the covariance of the data set as in Maze, Mercier, Fablet, et al. (2017). We modified their data preparation procedure to include both temperature and salinity. Our procedure is as follows:

- (1) Float in situ temperature was transformed into potential temperature ( $\theta$ ), and practical salinity into absolute salinity ( $SA$ ), using TEOS-10 (IOC et al., 2010). We have tested the method using practical salinity and  $\theta$ , which would be more consistent with TEOS-10, and found no differences in the results (not shown for brevity). Thereby, we decided to use the combination of  $\theta$  and  $SA$  for an easier comparison with previous works.
- (2) Profiles with valid QCed data between 300 and 900 m were selected. The upper 300-m limit is below most of the deepest mixed layer depths in this area (note that here the number of profiles with deep winter mixed layers, down to  $\sim 500$  m, are only a few tens, compared to thousands of profiles), which avoids influencing the classification algorithm by large seasonal variations. We have tested the algorithm using profiles with QCed data up to 50 m but found that 300 m resulted in a more correct profile classification (not shown for brevity). The lower 900-m limit is selected for the practical reason that most floats have continuous quality data above this depth: Extending the lower limit to a deeper depth would reduce the number of profiles that we can use for the study. Only 4% of the Argo profiles and none of the BGC-Argo profiles were rejected. It is possible to use the profiles to their individual maximum depths, but the missing values would need to be filled with, for example, the median of the data set or the most frequent value; this would create an unrealistic portion of the data set; thus, it is not an acceptable solution nor necessary.
- (3) We normalized each property measurement,  $i$ , by the property standard deviation calculated at each 1-dbar level:  $\theta_{i,n} = (\theta_i - \mu_\theta) / \text{std}(\theta)$  and  $SA_{(i,n)} = (SA_i - \mu_{SA}) / \text{std}(SA)$ , where  $\mu_\theta$  and  $\mu_{SA}$  are the depth-dependent averages of  $\theta$  and  $SA$ , respectively, across the Argo float profiles, and  $\text{std}(\theta)$  and  $\text{std}(SA)$  are their depth-dependent standard deviations.
- (4) Following Maze, Mercier, Fablet, et al. (2017) and Jones et al. (2018), we reduced the vertical dimensionality of the problem (1-dbar data create 600 vertical dimension points) by decomposing the Argo and BGC-Argo data set using principal component analysis (PCA) applied to the 300- to 900-m layer. A PCA decomposition is a common method used in climate science and machine learning to detect the main covariance patterns in the data and reduce the number of dimensions. We found that  $\sim 99\%$  of the property variance of  $\theta$  and  $SA$  can be explained by their respective first 2 PCAs (Figure S2 in the supporting information), which are then used to reduce the profile dimension from 1,200 points (i.e., 600 depth levels for  $\theta$  and 600 for  $SA$ ) to four points (i.e., the two modal amplitudes for  $\theta$  and two for  $SA$ ). These four points are the inputs for the classifier algorithm. Note that, compared to Maze, Mercier, Fablet, et al. (2017) and Jones et al. (2018), we found a smaller number of PCAs, which explains the variability of our profiles. This is mainly due to the fact that we apply the algorithm to a only a portion of the full vertical range of the profiles (i.e., this range does not capture the deeper water masses nor the surface ones), which decreases the number of modes needed.

- (5) To assure an optimal and unbiased coverage of the analysis domain we selected a random profile in every  $0.1^\circ \times 0.1^\circ$  box, similar to Jones et al. (2018), to be used for the classifier algorithm training set. This corresponds to 87,032 profiles, or  $\sim 89\%$  of the Argo data set for this region.
- (6) The standardized and reduced  $\theta$  and  $SA$  data were combined together in the same array  $\vec{X}$  of dimensions  $4 \times 87,032$ . The Gaussian Mixture Model algorithm then computes the optimal (i.e., the set of parameters maximizing the likelihood of all the data belonging to one of the clusters. This is computed using an Expectation-Maximization algorithm; see Maze, Mercier, Fablet, et al., 2017, for more details.) Gaussian weights  $\lambda_k$ , mean  $\mu_k$  and covariance  $\Sigma_k$  allowing one to compute the probability of a profile  $x \in \vec{X}$  belonging to each “component”  $k$  of the Gaussian mixture:

$$p(k|x) = \frac{\lambda_k \mathcal{N}(x; \mu_k, \Sigma_k)}{\sum_{k=1}^K \lambda_k \mathcal{N}(x; \mu_k, \Sigma_k)} \quad (1)$$

where a Gaussian distribution  $\mathcal{N}$  is given by:

$$\mathcal{N}(x; \mu_k, \Sigma_k) = \frac{1}{\sqrt{(2\pi)^D |\Sigma_k|}} \exp\left(-\frac{1}{2}(x - \mu_k)^\top \Sigma_k^{-1} (x - \mu_k)\right), \quad (2)$$

with  $|\cdot|$  the determinant and  $T$  the transpose operators.

- (7) The sum over all components of the  $p(k|x)$  is 1. The Gaussian mixture model is thus a probabilistic classifier, but note that each profile can be attributed to the component  $k$  for which the  $p(k|x)$  is maximum. The relative amplitudes of the  $p(k|x)$  are then used to assess the robustness of the classification.
- (8) Assessment of the classification is a fundamental step and can require subjective adjustments of the results (see an example in section 5.1).

We performed several tests, using only one property (either  $\theta$  or  $SA$ ), or a combination of the different properties ( $\theta$ ,  $SA$ , nitrate, and pressure), or single depth data (e.g.,  $\sim 50$  and  $\sim 200$  m), to reduce dimensionality instead of eigenvectors; but the combination of the first two PCAs of  $\theta$  and  $SA$  was found to be the best choice, as this allows a definition of clusters that automatically capture most of the Southern Ocean regimes. In particular, in the subtropical and the southernmost zones, where salinity plays a fundamental role in setting the stratification, using temperature-only data would not correctly classify these areas. We also tested the PCM approach using an alternative classifier: the  $k$ -means algorithm, which assigns each profile to only one cluster  $k$ , based on the Euclidean distance of the profile to the nearest cluster mean (Hartigan & Wong, 1979) but found that  $k$ -means poorly separates the data in the southernmost regions.

Both PCA analysis and the Gaussian Mixture Model were performed using the Python scikit-learn Version 0.20 machine learning package (Pedregosa et al., 2011). Our code was adapted from the pyXpcm software (<https://pyxpcm.readthedocs.io>), a Python implementation of PCM (Maze, Mercier, & Cabanes, 2017). The Gaussian Mixture Model used a “full” covariance matrix and nine clusters (or components  $k$ ). We tested the number of clusters between 5 and 15 and ultimately chose 9 as it allowed for a meaningful separation of the profiles into the desired Southern Ocean regimes. While there is no perfect way to choose between different numbers of clusters, we have validated this choice by looking at the Bayesian information criterion (Konishi & Kitagawa, 2008; Schwarz et al., 1978), computed using 10 sets of randomly selected profiles, with a total number of 2,166 profiles ( $\sim 2.2\%$  of the data set). Although a clear minimum does not appear (as already found by Jones et al., 2018), the method suggests an optimum value of between 9 and 15 clusters (see Figure S3 in the supporting information).

### 4.3. Spatial Variability of Water Masses

To describe how properties change with longitude, with respect to the location of KP and across the five regimes, we define four regions: west ( $0\text{--}40^\circ\text{E}$ ), upstream ( $40\text{--}68^\circ\text{E}$ ), downstream ( $68\text{--}120^\circ\text{E}$ ), and east ( $120\text{--}180^\circ\text{E}$ ) of KP. These four regions identify different regimes of eddy kinetic energy both at the surface (Sallee et al., 2011) and at 1,000-m depth (Roach et al., 2018). The properties are investigated in the intermediate (section 5.3) and deep water masses (section 5.4). In order to focus on the variability associated with specific water masses and remove the effect of isopycnal heave, we analyze the profiles in  $\Sigma_0$  coordinates (i.e., anomaly of density, with respect to a reference pressure of 0 dbar, from  $1,000 \text{ kg/m}^3$ ). We use a resolution of  $0.03 \text{ kg/m}^3$  between the  $25.4\text{--}27.5\text{-kg/m}^3$  isopycnals, and a  $0.01\text{-kg/m}^3$  step for denser classes, which resolves the density variations in both the upper and deep ocean.

In order to investigate the major hot spots of the variability associated with each property, we also compute the ratio of the AAIW (or UCDW) property variance in  $2^\circ$  longitude bins and the total AAIW

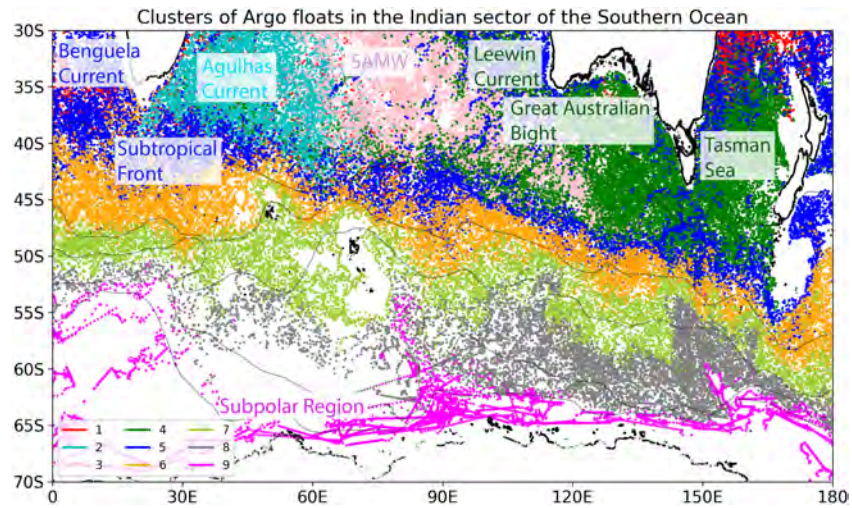


**Figure 2.** Spatial distribution of the nine clusters (colors) overlaid on bathymetry (grayscale map; ETOPO1 Amante & Eakins, 2009) in the Indian sector of the Southern Ocean. Clusters were identified by the Profile Classification Model method using the full Argo data set. The five Orsi et al. (1995) fronts are indicated by black contours, as in Figure 1.

(UCDW) property variance (computed for the whole domain, from 0° to 180° longitude):  $\frac{\text{var}(C)_{2\sigma}}{\text{var}(C)_{tot}}$ , where  $C = \{SA, \theta, O_2, NO_3^-, pH\}$ .

## 5. Results

### 5.1. Resulting Argo Profile Clusters

The resulting nine Argo clusters are shown in Figure 2 ordered from north to south, where climatological fronts (Orsi et al., 1995) are plotted in black for reference. The classification captures a roughly meridional structure from south of the STF through the ACC that resembles the Orsi et al. (1995) frontal zones. North of the STF, the subtropical waters are classified into five distinct, quasi-zonal groups: the Agulhas Current region ( $k = 2$ ), the SAMW pool in the central subtropical gyre ( $k = 3$ ), the Australian currents system including the Tasman Sea, Great Australian Bight, and Leeuwin Current region ( $k = 4$ ), and the STF, together with the Benguela Current and waters around Australia, at  $k=5$ . Clusters 6–8 identify the ACC waters, while Cluster 9 depicts subpolar waters that also comprise the seasonal SIZ. Our classification compares well with

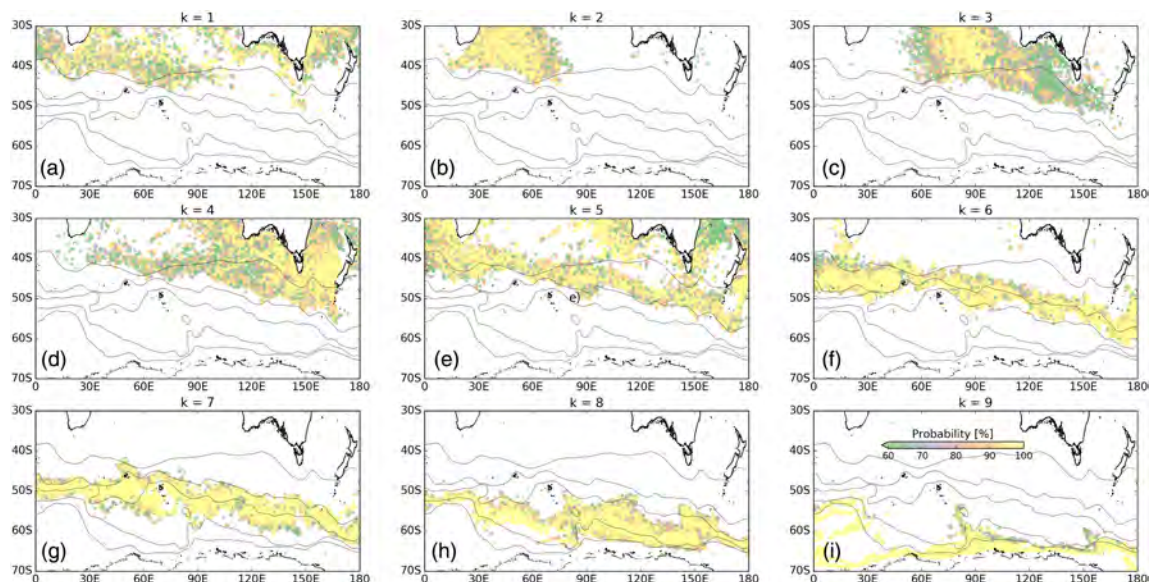


**Figure 3.** Posterior probability (%) (colors) associated with each of the (a–i) nine clusters ( $k$ ) shown in Figure 2. A color bar is shown in panel (i). The Orsi et al. (1995) fronts (black contours) are shown for reference.



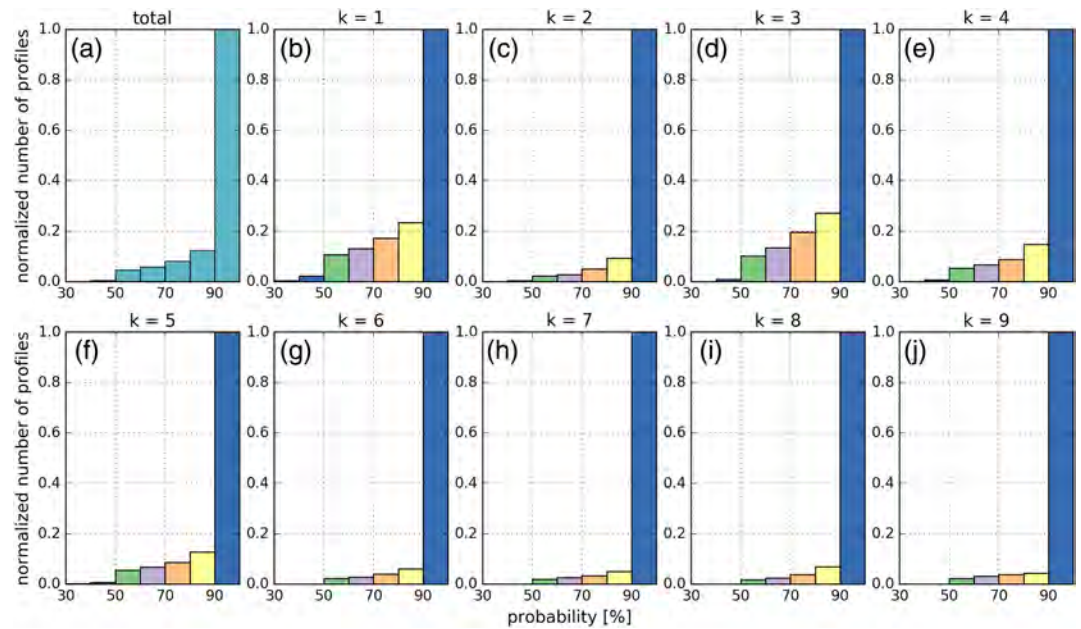


**Figure 4.** Histograms of the percent posterior probability associated with (a) the full Argos data set and (b–j) each of the nine clusters ( $k$ ) presented in Figure 2. The number of profiles for each 10% bin is normalized by the total number of profiles in the 90–100% bin and are color coded in panels (b)–(j).

the eight clusters found by Jones et al. (2018) for the entire Southern Ocean. The biggest difference is north of the STF, where our approach separates the Agulhas waters from the central and eastern Indian Ocean (SAMW and Australian waters).

The posterior probability, given as % value, is mostly large (more than 80%) for each cluster (Figures 3 and 4). However, some profiles (more than 20% of the total number) in each classification component have a probability  $\leq 70\%$  and a corresponding probability of  $\geq 30\%$  in a contiguous cluster, in particular, in  $k = 1, 3, 4,$  and  $5$  (Figure 5). These profiles tend to be concentrated in areas of strong currents (such as the Agulhas Return Current in Cluster 4; the East Australian Current in Clusters 1 and 5; the large air-sea

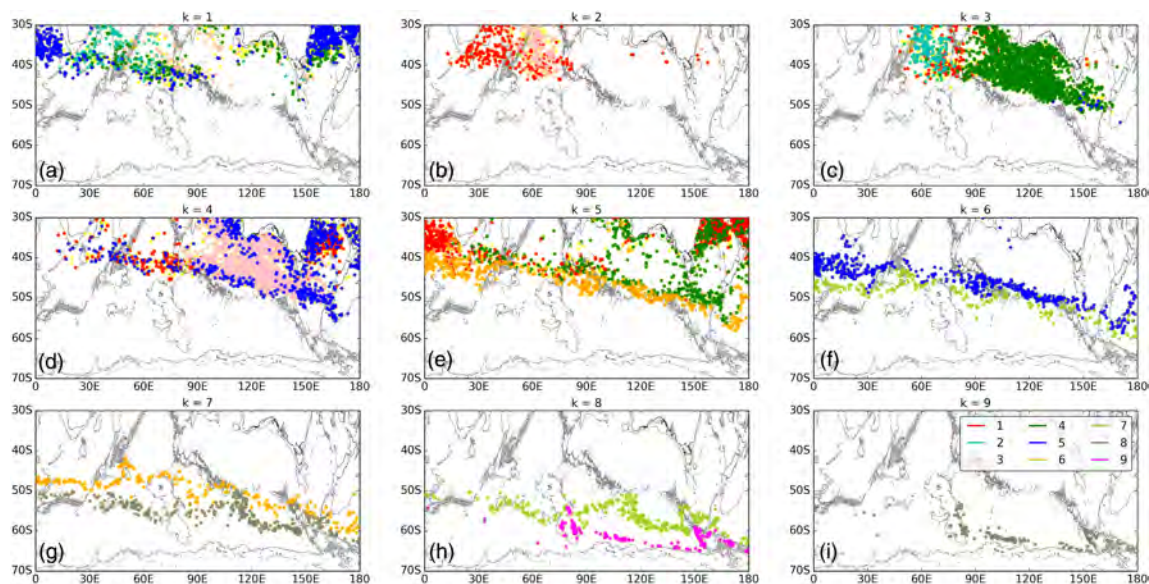


**Figure 5.** (a–i) Profiles with a posterior probability less than 70%. Those profile that have a probability of more than 30% to belong to the remaining clusters are color coded as in legend in panel (i). In yellow are those profile that do not have a probability of  $\geq 30\%$  for the remaining clusters. Black contours are coastlines and the 3,000-m isobath (bathymetry from from ETOPO1 Amante & Eakins, 2009).

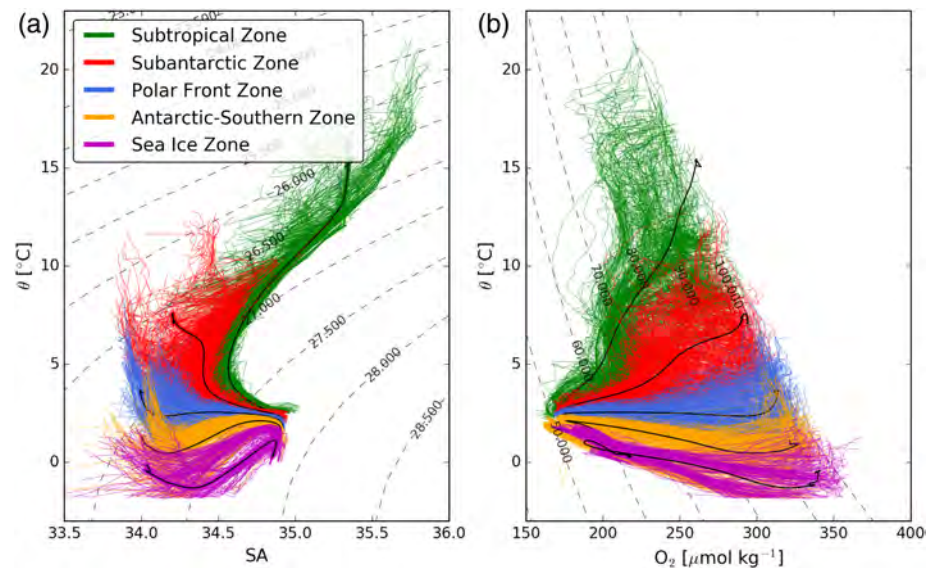


**Figure 6.** BGC-Argo profiles colored by Southern Ocean regime as a function of (a)  $\theta$ -SA and (b)  $\theta$ - $O_2$ : Subtropical Zone (STZ; green), Subantarctic Zone (SAZ; red), Polar Frontal Zone (PFZ; blue), Antarctic-Southern Zone (ASZ; orange), and Sea Ice Zone (SIZ; magenta). The black contours indicate the mean Argo profile by frontal zone. Dashed lines in (a) show  $\Sigma_0$  contours, while in (b) % of oxygen saturation.

exchange and deep mixed layers in the SAMW formation sites of Clusters 3 and 4; the Southern Ocean fronts in Clusters 7–9), and in the SAZ (Cluster 6). The ambiguity in the classification comes from adjacent clusters and is therefore unlikely to be due to a missing cluster to define these points. In order to confirm this assertion, we have calculated the same metric using a larger number of clusters (i.e., 15) and found no discernible difference with Figure 5 (not shown). Thus, we do not discard any point with low probability, as this may be indicative of strong eddy and frontal dynamics or of seasonal and interannual variability (Jones et al., 2018).

### 5.1.1. Southern Ocean Zones

The variability of the waters in the Indian sector of the Southern Ocean is examined in terms of potential temperature, salinity, dissolved oxygen, nitrate, and pH. In particular, we identify the variability for specific water masses (1) across fronts and (2) driven by the presence of the KP, as this large topographic feature is a site of convergence of upper, intermediate, deep, and bottom waters (Donohue et al., 1999; Fukamachi et al., 2010; Park, Roquet, et al., 2008; Tamsitt et al., 2017). In order to identify specific water bodies, such as the AAIW or the UCDW, we first classify each profile of the Argo and BGC-Argo data set by its Southern Ocean regime and then select the associated density class.

We define four Southern Ocean zones by grouping together some of the nine clusters identified in Figure 2, based on the  $\theta$ -SA of each cluster (not shown): the STZ (green profiles in Figure 6, the set of all profiles with  $k$  in the range 1 to 5), SAZ (red,  $k = 6$ ), PFZ (blue,  $k = 7$ ), ASZ (orange,  $k = 8$ ), and SIZ (magenta,  $k = 9$ ). The resulting classification of the Southern Ocean regimes south of the PF (PFZ, ASZ, and SIZ) is not affected by the number of clusters ( $k$ ) from 5 to 15 (not shown). However, the classification is sensitive to the choice of  $k$  in the SAZ and especially in the STZ (not shown), where for  $k < 9$  the algorithm grouped the southernmost STZ profiles in the SAZ.

The PCM highlights areas of mixing between regions, where profiles show marked intrusions of waters in the upper ocean. An example of these intrusions is shown by the intense interleaving of temperature and salinity layers found in the profiles of BGC-Argo float with World Meteorological Organization ID #5904676 (Figure 7). These interleaving structures indicate the occurrence of mixing and intrusions due to cross-frontal exchange, facilitated by vigorous eddy activity at the location of the front (Llort et al., 2018; Park et al., 1993). These features are found both in the upper ocean (dashed lines in panel b, corresponding to the two markers in panel a and to the warmer and saltier intrusion of waters at 100–400 dbar in panels c and d) and at the salinity minimum of the AAIW (values at potential density anomalies  $\Sigma_0$  between 27 and 27.2  $\text{kg/m}^3$  in panel b). The interleaving here occurs when the fresher and colder Subantarctic Surface

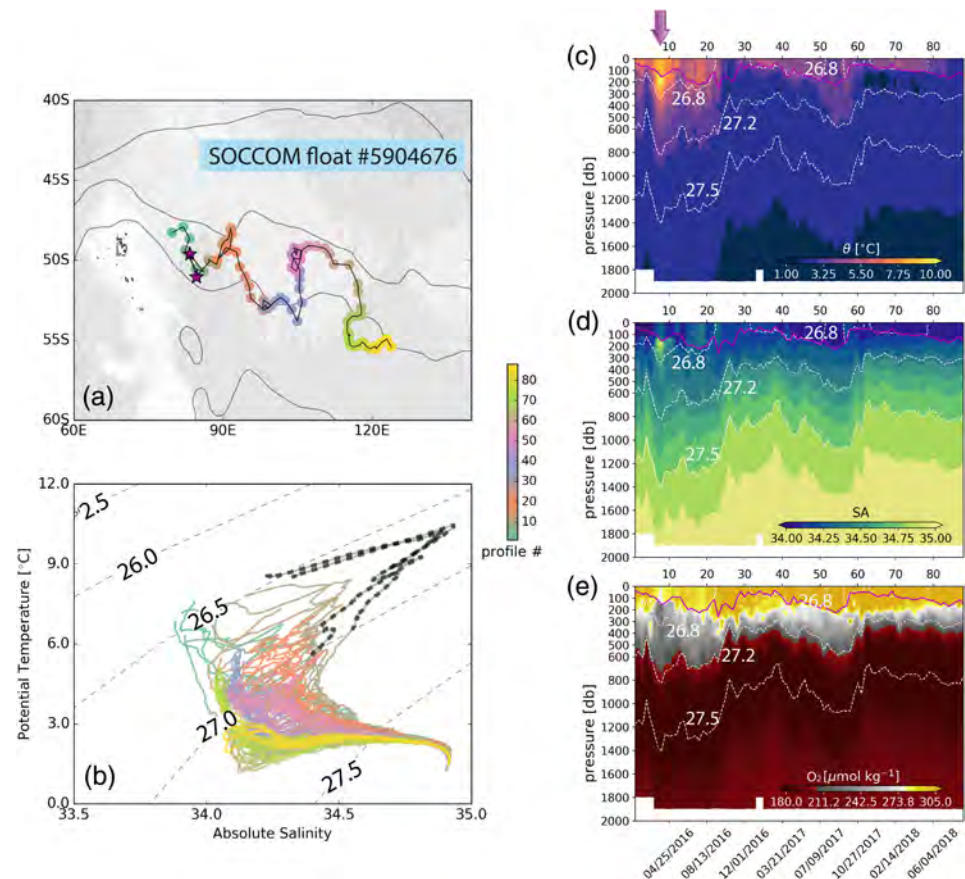


**Figure 7.** The (a) sampling trajectory and (b)  $\theta$  and SA properties of biogeochemical-Argo Float #5904676, colored by profile number (out of total 88), which collected (c) potential temperature, (d) absolute salinity, and (e) dissolved oxygen of the upper 2,000 m, between January 2016 and June 2018. Note the two intrusion events (red stars in panel a and dashed black lines in panel b) are identified in Profiles #8 and #9, magenta arrow in panels c–e). Bathymetry (grayscale map; ETOPO1 Amante & Eakins, 2009) and Orsi et al. (1995) fronts are indicated in (a) as in Figure 1. Dashed white contours in panels (c)–(e) are  $\Sigma_0$  isolines, with values indicated in white.

Water comes into contact with the warmer and more saline water of the Agulhas Return Current, originating from the Agulhas Current and encountering ACC waters north of Crozet Plateau ( $\sim 53^\circ\text{E}$ ) first, and then at KP (Park et al., 1993; Sallée et al., 2010).

The PCM method captures a feature in the area west and southwest of South Africa (in the Agulhas rings and the Benguela current, Figure 2), in Cluster 6 at  $\sim 30\text{--}35^\circ\text{S}$ ,  $\sim 10\text{--}20^\circ\text{E}$ , which should be grouped within STZ waters, according to its  $\theta$  and SA properties (Figure 6). Most of the profiles of this cluster shows high posterior probability (Figure 6a) and thus cannot be discarded. The  $\theta$ -SA diagram in Figure 6 shows that at latitudes close to  $37^\circ\text{S}$  (panel b), the surface waters (c) have temperatures warmer than  $14^\circ\text{C}$ , even in winter months (yellow colors in panel d), typical of subtropical waters in this region (Park et al., 1993). Thus, because of their upper ocean structure, we rely on a subjective definition and classify these profiles within the STZ. We find that this feature is independent of the choice of  $k$  (not shown) and highlights an interesting connection at levels below 300 m (i.e., an undercurrent), between ACC waters and the region south and southwest of South Africa, which may indicate a pathway of intermediate and deep waters. This is not an error of the PCM method, as the PCM here captures similarities across data that connect intermediate waters from the ACC, but we decided to manually separate these points from the SAZ, because of the usual classification of Southern Ocean zones.

Profiles with interleaving in the upper ocean are also found at warmer temperatures (not shown), likely due to either the passage of meanders and eddies of the SAF, by the proximity (and in some cases the merging) of the SAF and STF in some locations of the South Indian Ocean: close to  $\sim 30^\circ\text{E}$ , near the Crozet Islands ( $\sim 53^\circ\text{E}$ ), north of KP, east of  $\sim 125^\circ\text{E}$  on the northern flank of the Southeast Indian Ridge

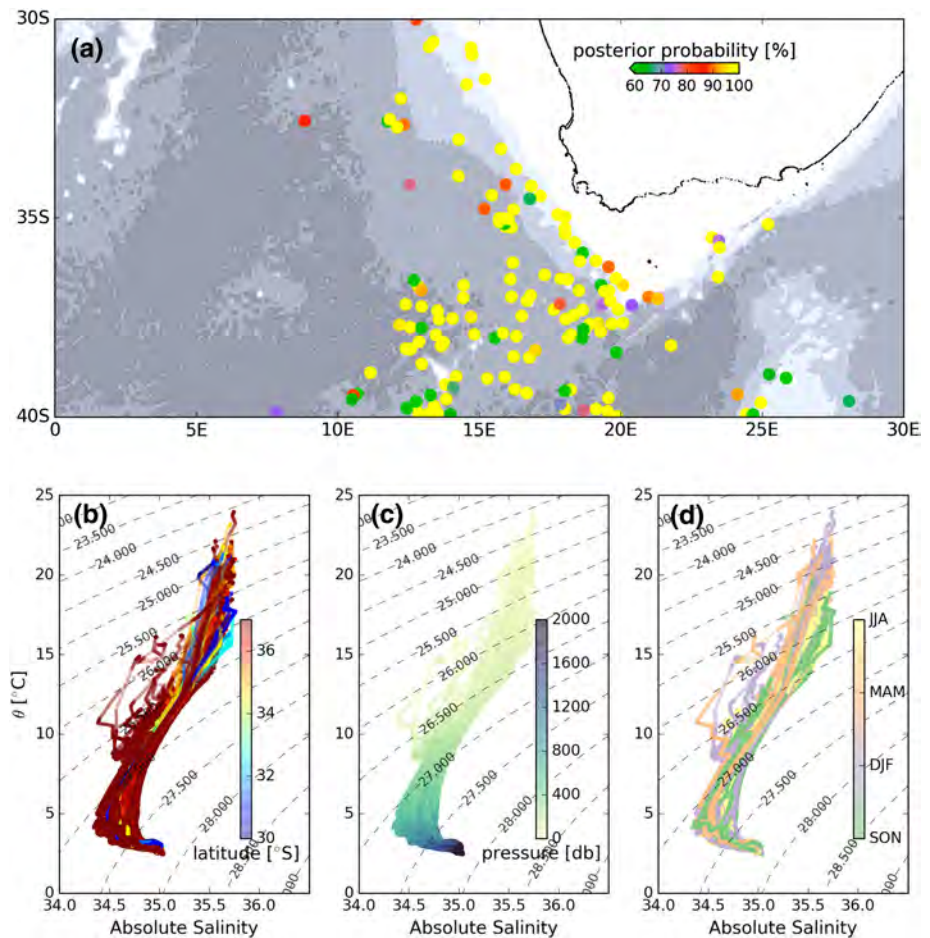


**Figure 8.** (a) Percent posterior probability (colors) and (b–d)  $\theta$  and SA properties of subtropical profiles classified within the Subantarctic Zone (cluster  $k = 6$ ) off the coast of Africa.  $\theta$  and SA diagrams are colored by latitude in (b), pressure in (c), and season in (d).

(Freeman & Lovenduski, 2016; Moore et al., 1997; Park et al., 1993; Read & Pollard, 1993), or to drifting floats crossing a front. Of this type of interleaving, we find a group of profiles (Figure 6) with an upper thermohaline structure with temperatures warmer than 14 °C and salinity larger than 34.7, which are typical of Subtropical Surface Water, rather than Subantarctic Surface Water of the upper SAZ (Orsi et al., 1995; Talley et al., 2011). Therefore, we manually group these waters into the STZ. Yet the advantage of the PCM approach is to use an algorithm that efficiently and automatically classifies a large number of data, without defining specific rules for each case. It is therefore beyond the scope of the present work to check every profile that could fall into this case, so we rely instead on a probabilistic approach.

The final Argo and BGC-Argo profile classification in Southern Ocean regimes used in this study is shown in Figure 8. The classification shows generally a good comparison between the instantaneous margins of the STZ, SAZ, PFZ, ASZ, and SIZ and the climatological STF, SAF, PF, and the southern boundary of the ACC (black contours Orsi et al., 1995), except for the STF east of 80°E. Qualitatively, the location of the different zones is also aligned with the areas delimited by the fronts identified by Sokolov and Rintoul (2009b) (not shown), where front locations are based on sea surface height. However, the temporal variability of the fronts is also large, as discussed in Sokolov and Rintoul (2009a) and Freeman et al. (2016), which could in part explain the largest misfit between the PCM zones and the climatological zones defined by Orsi et al. (1995). Other regime-front mismatches may be due to the methodology for detecting a front's location, especially in proximity of complex topography (Sokolov & Rintoul, 2009b; Sparrow et al., 1996) (Figure 9). In particular, the SAF and the PF have been shown to differ significantly in the Indian sector of the Southern Ocean, especially near Crozet Plateau and KP (e.g., Freeman & Lovenduski, 2016; Orsi et al., 1995; Park et al., 2009; Sokolov & Rintoul, 2009a).

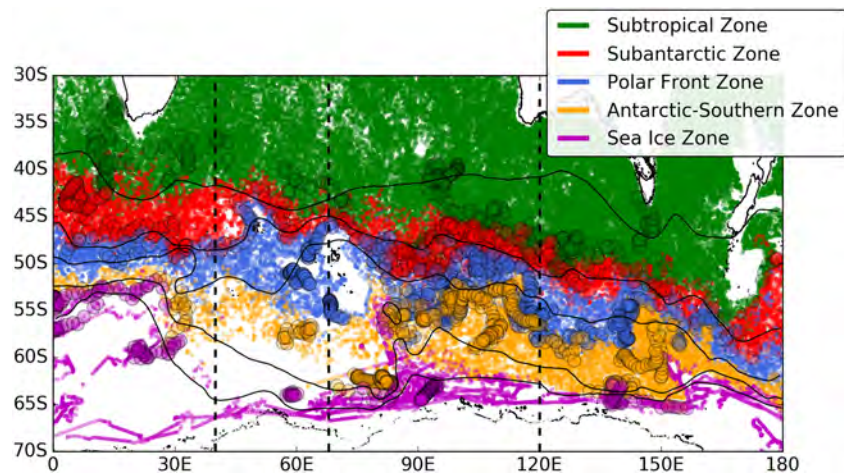


**Figure 9.** Argo (colored dots) and biogeochemical-Argo (larger, outlined colored circles) float profile locations colored by Southern Ocean frontal zone: Subtropical, Subantarctic, Polar Frontal, Antarctic-Southern, and Sea Ice Zones. Profiles are classified using the Gaussian Mixed Models algorithm applied to potential temperature and absolute salinity measurements (see section 4). We define four regions relative to the Kerguelen Plateau by longitude (delineated by vertical dashed black lines): west (0–40°E), upstream (40–68°E), downstream (68–120°E), and east (120–180°E). For reference, gray contours indicate the location of the five Orsi et al. (1995) fronts.

The distinction between the different regimes is also evident in the mean float-based vertical profiles of  $\theta$  and SA (Figure 10). Here, we can see a net gradient in all the properties, both in the upper and deep ocean (except for salinity, as the ACC is the freshest), with a transition from the warmest and saltiest STZ waters to the coldest and fresher SIZ waters (panel a, blue, orange, and magenta lines), the upper ocean waters are very cold and fresh (Antarctic Surface Water) and show the typical subsurface temperature minimum of the Winter Water south of the PF, which is the remnant of the cold winter waters (Talley et al., 2011). At depth, the salinity minimum in the SAZ and PFZ is well captured, around 500 and 1,000 m, respectively (Figure 10b). Furthermore, property variability, shown as the variance computed over each regime, is largest in the upper water column and at intermediate depths (~1,000 m).

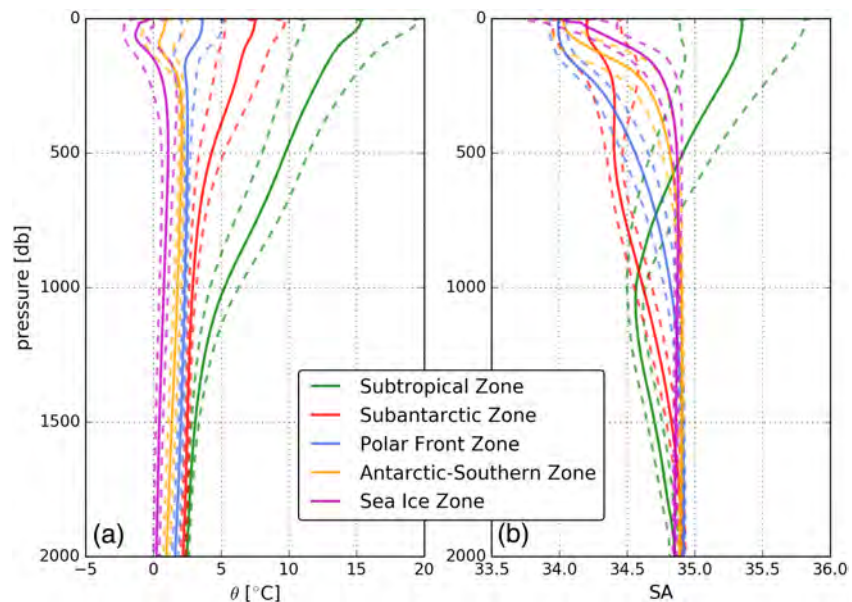


**Figure 10.** Vertical mean (solid) and one standard deviation (dashed) of (a) potential temperature and (b) absolute salinity of all Argo profiles from the Indian sector of the Southern Ocean used in this study. Metrics are colored by Southern Ocean frontal zone: Subtropical Zone (green), Subantarctic Zone (red), Polar Frontal Zone (blue), Antarctic-Southern Zone (orange), and Sea Ice Zone (magenta).

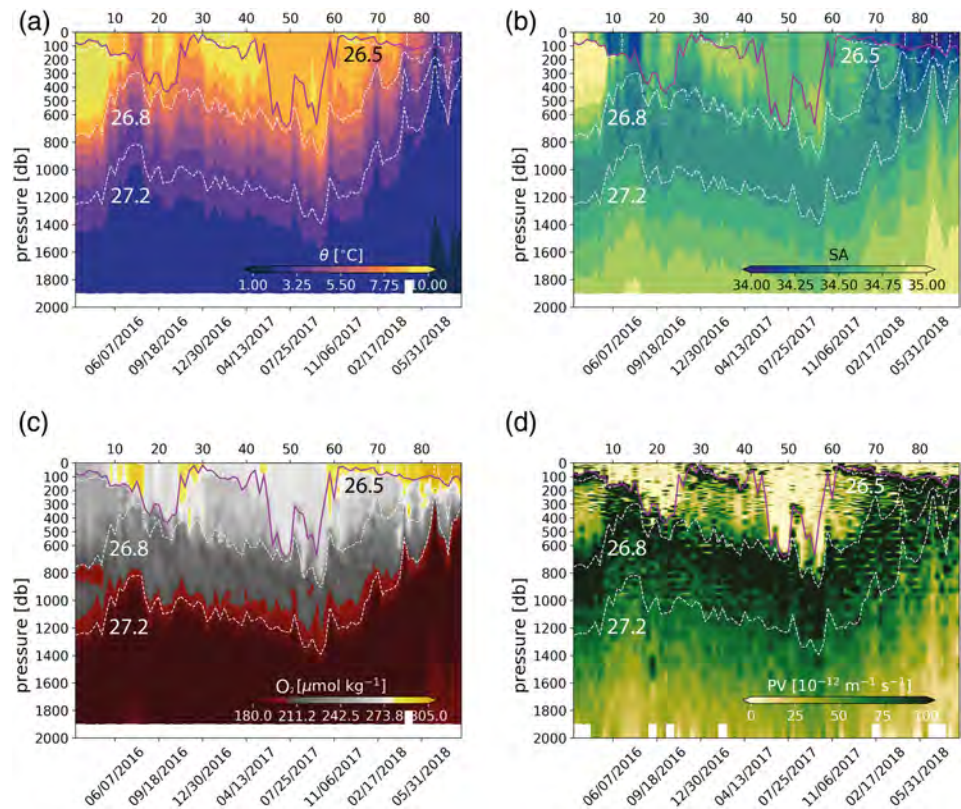


**Figure 11.** Upper 2,000 m (a)  $\theta$ , (b) SA, (c) dissolved oxygen, and (d) potential vorticity of biogeochemical-Argo Float #5904688. Dashed white lines are  $\Sigma_0$  isolines, with values indicated in white.

This variability is due to the seasonal and interannual variability of the profiles but may also reflect some mixing and interleaving.

Selecting only the BGC-Argo profiles, the distinction between the different zones is evident in the  $\theta$ -SA and  $\theta$ - $O_2$  property diagrams (Figure 6), with the oxygen increasing in the surface waters from the STZ toward Antarctica and with a minimum in each regime, which characterizes the UCDW core.

To highlight the effect of KP, in the following sections, we will describe how the properties associated with the four Southern Ocean regimes (STZ, SAZ, PFZ, ASZ, and SIZ) vary as a function of longitude.

## 5.2. SAMW Floats

Compared to the full Argo data set used in this study, the BGC-Argo floats only marginally capture the SAMW formation pool in the southeast Indian Ocean region (see Aoki et al., 2007; Sallée et al., 2006, for maps of SAMW pool distribution in this region). Hence, a complete discussion of the BGC property variability associated with this water mass and the influence of the ocean circulation on the SAMW is not possible. Instead, a description of the local properties captured by the BGC-Argo floats is given here.

BGC-Argo Floats #5904688 (UW 9600), #5904683 (UW 9650), #5904682 (UW 9637), and #5904675 (UW 9749) (see Table S1 and Figure 1) show the presence of SAMW formation in the wintertime deep mixed layers, in the  $\Sigma_0$  range between 26.65 and 26.85  $\text{kg}/\text{m}^3$ . For example, Figure 11 shows the vertical sections of  $\theta$  (a), SA (b),  $O_2$  (c), and PV (d) ( $PV = -\frac{f}{\rho} \frac{\partial \rho}{\partial z}$ , where  $f$  is the Coriolis parameter and  $\rho$  is the density) for Float #5904688 (UW 9600). Between mid-June and mid-September 2016 and 2017, the winter mixed layer, computed using a density criterion of  $\Delta\Sigma_0 = 0.03 \text{ kg}/\text{m}^3$ , develops the typical deep values of approximately 400–700 m associated with SAMW formation. The temperature and salinity are well mixed in this volume of water (panels a and b), the oxygen concentration is high, with values around 270  $\mu\text{mol}/\text{kg}$  (c), and the PV (d) is, as expected, very low ( $\sim 20 \times 10^{-12} \text{ m}^{-1} \cdot \text{s}^{-1}$ ).

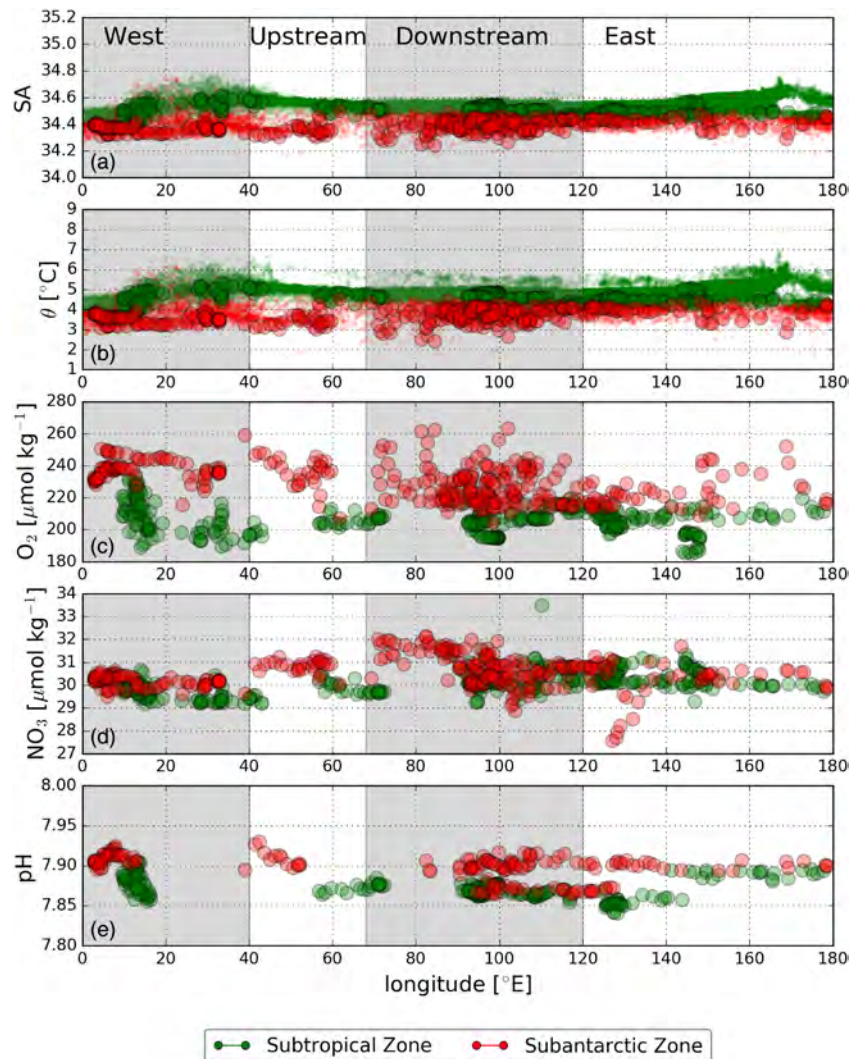


**Figure 12.** (a) Absolute salinity, (b) potential temperature, (c) dissolved oxygen, (d) nitrate, and (e) dissolved inorganic carbon, as measured by core Argo (colored dots) and biogeochemical-Argo (outlined colored circles) floats across the northernmost frontal zones, the (green) Subtropical Zone and (red) Subantarctic Zone. Properties are averaged over the Antarctic Intermediate Water layer (with density between  $\Sigma_0 = 27$  and  $27.2 \text{ kg/m}^3$ ).

### 5.3. Property Variability of the Intermediate Waters

We identify AAIW using  $\Sigma_0$  between  $27.1$  and  $27.3 \text{ kg/m}^3$  (Figure 6 Talley et al., 2011) and investigate its zonal variability in the STZ and SAZ and at depth (Figure 12). AAIW properties in the figure are averaged across the AAIW density class and have a distinct meridional gradient, with saltier, warmer, and lower oxygen waters in the STZ than in the SAZ. The core Argo and BGC-Argo results are comparable, as they should be since BGC-Argo is a subset of core Argo. Both show larger variability in the SAZ than in the STZ. Between  $20$ – $40^\circ\text{E}$  and  $145$ – $180^\circ$ , the core Argo float data show high salinity waters that come from the Agulhas Current and the subtropical waters east of Australia, regions where BGC-Argo floats are not present. In the STZ, the largest difference in  $\theta$  between the core and the BGC-Argo data ( $20$ – $180^\circ\text{E}$ ) is due to the warmer subtropical waters present in the northernmost region where there are no BGC-Argo floats (Figure 9).

The largest oxygen concentration in the STZ ( $\sim 230 \mu\text{mol/kg}^3$ ) is found in the upstream region, west of  $20^\circ\text{E}$ . East of this location, the oxygen concentration in the STZ is overall lower. The SAZ shows larger values (more than  $260 \mu\text{mol/kg}^3$ ) and spread for the oxygen concentration in the downstream region, up to longitudes  $\sim 100^\circ\text{E}$ , east of which the oxygen concentration first decreases and then rises again east of approximately  $150^\circ\text{E}$  (nearly  $260 \mu\text{mol/kg}^3$ ). Larger oxygen concentration in the SAZ is consistent with the vicinity to source

waters. The largest changes in the SAZ oxygen concentration are  $\sim 52 \mu\text{mol}/\text{kg}^3$ , found in the downstream region. Since the seasonal cycle is well captured in both the core and the BGC-Argo data sets, the difference might be due to local mixing and interannual variability.

Nitrate concentration in the STZ has larger values in the East region, with an overall range between 29 and  $31.5 \mu\text{mol}/\text{kg}^3$ , with the maximum increasing toward the east. We notice a large nitrate concentration ( $\sim 33.5 \mu\text{mol}/\text{kg}^3$ ) at approximately  $110^\circ\text{E}$  (Figure 12), more similar to values found in the SAZ. This is an indication of the mixing across the STF and intrusion of STZ waters, which create some ambiguity in the PCM classification of temperature and salinity profiles. In the SAZ, again we notice the largest concentration and spread in the downstream region, with a maximum nitrate concentration of  $32.2 \mu\text{mol}/\text{kg}^3$  and a change in nitrate concentration of approximately  $3.5 \mu\text{mol}/\text{kg}^3$ . East of the downstream region, the nitrate concentration decreases again, to values similar to those found in the west and upstream regions (about  $31 \mu\text{mol}/\text{kg}^3$ ). We notice a group of data points in the east region (east of  $125^\circ\text{E}$ ), with values less than  $29 \mu\text{mol}/\text{kg}^3$ , which could be indicative of, as in the previous case, ambiguity in the classification or intrusion of low-nitrate waters. This location corresponds to the Australian-Antarctic discordance, a deep and rough section of the Southeast Indian Ridge that allows the passage of Antarctic Bottom Water (e.g., McCartney & Donohue, 2007). Lower values of nitrate here may be indicative of intrusion of low-nitrate waters through the discordance.

The pH sensors mounted on some floats failed ([https://socom.ucsd.edu/floats/SOCCOM\\_sensor\\_stats.html](https://socom.ucsd.edu/floats/SOCCOM_sensor_stats.html)), so the spatial coverage of pH data is not as dense as for the other parameters, neither in the STZ nor in the SAZ waters. However, we notice that the STZ pH is overall lower than in the SAZ, except around  $100^\circ\text{E}$  in the downstream region and further in the east region, east of  $140^\circ\text{E}$ . At  $100^\circ\text{E}$  two distinct regimes appear: This could be due to the more limited sampling coverage of pH compared to other properties, due to sensor failure. However, BGC properties are found to have different gradients and fronts, compared to temperature and salinity (see, e.g., the difference between the nutrient and physical fronts found by Freeman et al., 2019). Investigating what drives the difference between pH and nitrate is left for future work, which would require considering the frontal structure of the BGC fields, together with the temperature and salinity fronts. As mentioned above, the property variability in the STZ waters, depicted by the spread of the values in Figure 12, is smaller than the variability in the SAZ. The variability for both zones is zonally dependent, with larger spread in the downstream region for each property, and neither shows an impact due to seasonality (not shown). As previously stated, we note that for those profiles with signatures of mixing (associated with water characteristics that are intermediate between two adjacent regimes), the PCM classifier algorithm may not robustly distinguish the profiles' regime (Figure 4). This can be indicative of leaking of fronts, where mixing is not instantaneous and can explain the similarity of some values in the STZ and SAZ noted in Figure 12.

The variability of AAIW in the STZ (Figure 13 red markers; the black line corresponds to the ratio of 1) shows a large hot spot in the west region, around  $10\text{--}30^\circ\text{E}$ , for SA (the core Argo  $\text{var}(SA)_{2\sigma}$  is more than twice as large than  $\text{var}(SA)_{\text{tot}}$ ,  $\theta$  (more than 1.5 times larger for both the Argo and BGC-Argo), and  $\text{O}_2$  (more than 1.5 times larger). The core Argo SA and  $\theta$  variance is large also in the east region, at about  $170^\circ\text{E}$ . The BGC-Argo does not capture the same magnitude of the Argo variance in the west region, likely due to the Agulhas current variability, which is not captured by the BGC-Argo profiles or by interannual variability. The variability in SA and  $\theta$  decreases with the longitude east of  $\sim 30^\circ\text{E}$  (i.e., away from the Agulhas current), in both the core and BGC-Argo ensembles. Finally, in the STZ oxygen, nitrate, and pH (despite the coverage in space being less dense than the other properties) show hot spots of binned variance larger than the total variance east of  $140^\circ\text{E}$ . Additionally, nitrate variance is larger in the downstream region, around  $110^\circ\text{E}$ .

The regional transition in the SAZ (Figure 13 cyan markers) highlights hot spots of larger variability (i.e., ratio  $> 1$ ) for salinity and temperature around  $70^\circ\text{E}$  between the upstream and downstream regions, then around  $80^\circ\text{E}$  and  $160^\circ\text{E}$  for both salinity, temperature, and oxygen.  $\text{NO}_3^-$  shows a slightly larger variability at  $60^\circ\text{E}$  in the upstream region, and between  $\sim 125^\circ\text{E}$  and  $145^\circ\text{E}$  in the east region. Finally, pH shows large variance in the eastern side of the downstream region ( $\sim 110^\circ\text{E}$  and in the east region, at approximately  $125^\circ\text{E}$ ).

#### 5.4. Property Variability of the Deep Waters

Circumpolar Deep Water (CDW) is found below AAIW in the STZ and SAZ and below Antarctic Surface Water south of the SAF. CDW is made up of an upper (UCDW) layer, characterized by an oxygen minimum



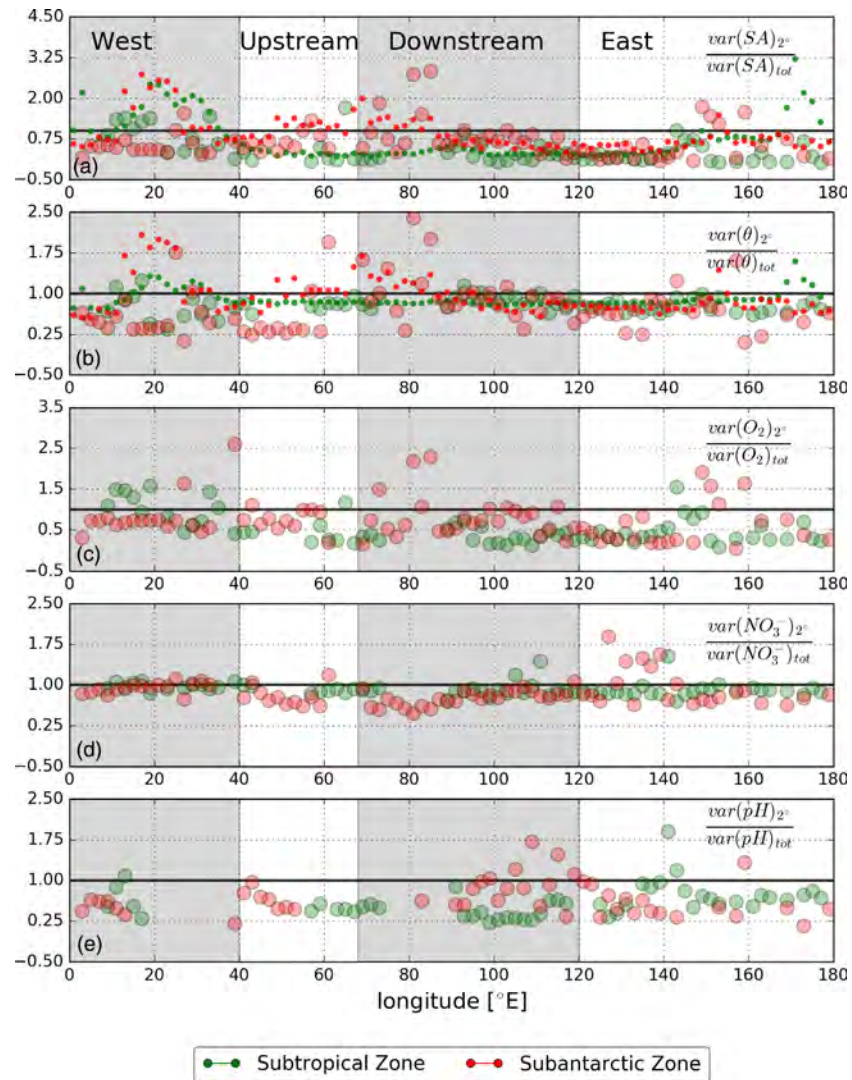


**Figure 13.** Regional variability of the ratio of binned ( $2^\circ$  in longitude) over the total variance of (a) absolute salinity ( $SA$ ), (b) potential temperature ( $\theta$ ), (c) oxygen ( $O_2$ ), (d) nitrate ( $NO_3^-$ ), and (e) pH, along  $\Sigma_0$ , computed across the density classes around the Antarctic Intermediate Water. Markers are color coded as in Figure 12.

centered around  $\Sigma_0 = 27.6 \text{ kg/m}^3$  (from Talley et al., 2011), and a lower CDW layer, with a typical salinity maximum ( $\Sigma_0 = 27.8\text{--}28.27 \text{ kg/m}^3$ , from Talley et al., 2011) originating from North Atlantic Deep Water. Because lower CDW is mostly found below 2,000 m and in the upper water only in the southernmost regimes, we here only analyze UCDW.

The average of the properties at densities  $27.6 \leq \Sigma_0 < 27.8 \text{ kg/m}^3$  is given in Figure 14. The values for the ASZ and the SIZ have been separated from the other zones for visualization purposes and are presented in the right panels of the figure.  $SA$  and  $\theta$  data are shown for both core (small markers) and BGC-Argo data (large markers), for comparison and statistics.

The meridional gradients of each property, from the STZ to the PFZ (left panels in Figure 14), are well defined, with increasingly colder UCDW waters poleward. In the downstream region, the meridional gradients switch sign: from the saltier, oxygen-rich, nitrate-poor, and higher pH waters of the west region (particularly in the STZ south west of South Africa), to fresher, oxygen-poor, nitrate-rich and pH low UCDW waters of the east region. We notice that the change is larger in the STZ than in the SAZ and PFZ. Very interesting is the larger spread associated with each of the properties in the PFZ downstream region, specifically in the area east of the KP, which is indicative of mixing processes. We also notice that in between the

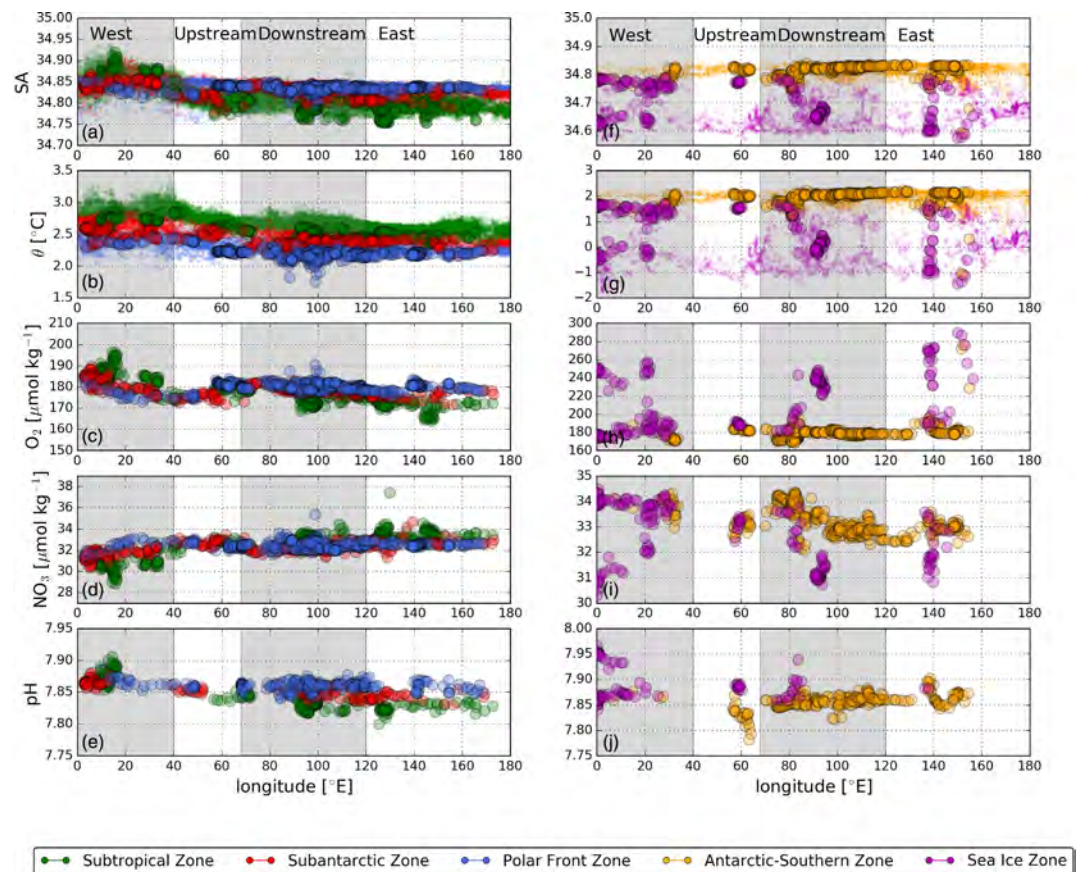


**Figure 14.** (a) Absolute salinity, (b) potential temperature, (c) dissolved oxygen, (d) nitrate, and (e) dissolved inorganic carbon, as measured by core Argo (colored dots) and biogeochemical-Argo (outlined colored circles) floats across the northernmost frontal zones, the (red) Subtropical Zone and (cyan) Subantarctic Zone. Properties are averaged over the Upper Circumpolar Deep Water (with density  $\Sigma_0$  larger than  $27.3 \text{ kg/m}^3$ ).

upstream and downstream regions the nitrate concentration is similar across the different Southern Ocean zones, with a difference in magnitude of approximately  $3 \mu\text{mol/kg}^3$ .

The southernmost zones (ASZ and SIZ) have the coldest and, in the SIZ, the most oxygenated UCDW waters. The range in each property values surpasses the northern zones, especially in the SIZ, because of the interaction of waters with the atmosphere and the formation/melting of sea ice. The largest ranges of the BGC-Argo data in the SIZ are found at  $0\text{--}20^\circ\text{E}$ ,  $80\text{--}95^\circ\text{E}$ , and  $140\text{--}155^\circ\text{E}$ , consistent with the core Argo data spread. The larger spread in the SIZ is indicative of the proximity with surface waters, as in these southernmost regions the UCDW upwells to the surface and interacts with the mixed layer (not shown for brevity). In particular, the higher oxygen in these zones can be explained by the temperature-driven higher solubility of these waters and by the springtime primary productivity in the SIZ, as a consequence of the melting of sea ice (Briggs et al., 2018). Note that a caveat of our analysis resides in the fact that the outcropping of UCDW can largely impact the property variance from surface processes rather than the interior mixing of water masses. To discern between surface processes and mixing events, one should remove the layers that interact with the mixed layers.

The large spread in the PFZ properties (left panels in Figure 14, blue markers) is likely a signature of mixing with ASZ and SIZ waters that are interacting with the surface. Whether any longitudinal property evolution or meridional property gradient between zones is the signature of strictly irreversible isopycnal transformations (isopycnal mixing) or results from a combination of isopycnal and diabatic processes (e.g., from the surface turbulent layer, topographic-induced turbulence, or other irreversible processes) can be explored using PV. Averaged over the depths of the UCDW density classes, PV shows three striking features (Figure 15): First, in the SAZ and the SIZ PV is much larger due to the interaction of UCDW with the atmosphere; second, PV shows hot spots of larger variability in the downstream region and around  $150^\circ\text{E}$  in the

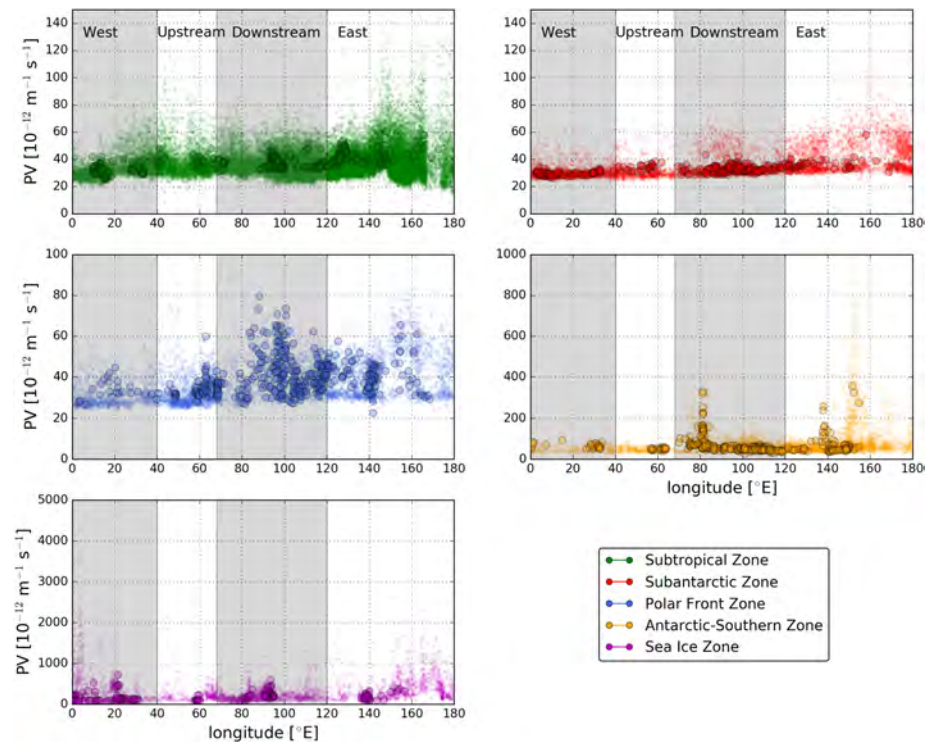


**Figure 15.** Potential vorticity along longitude, color coded by zone as in Figure 14 and averaged over the Upper Circumpolar Deep Water (with density  $\Sigma_0$  larger than  $27.3 \text{ kg/m}^3$ ).

PFZ, ASZ, and SIZ; and third, in the STZ, SAZ, and PFZ,  $PV$  has a positive trend toward the east. The various hot spots of larger  $PV$  variability and the  $PV$  trend are indicative of the presence of diabatic processes (Whalen et al., 2015) or air-sea interactions changing the UCDW density class stratification. Diabatic mixing of UCDW with the overlaying waters, which have greater  $PV$  (not shown), is facilitated by enhanced turbulence at topographic features such as KP.

We find several hot spots of larger property variability (computed as  $\frac{\text{var}(C)_{2^\circ}}{\text{var}(C)_{\text{tot}}}$ ) associated with the different zones (Figure 16). The BGC-Argo temperature and salinity variability compares well with core Argo. Nevertheless, we find differences in some locations, likely due to the poorer coverage in time and space of BGC-Argo. These differences are most noticeable in (1) in the STZ west of  $20^\circ\text{E}$ ; (2) in the SAZ upstream region; (3) between  $\sim 20^\circ\text{E}$  and  $80^\circ\text{E}$  in the PFZ; and (4) east of  $60^\circ\text{E}$  in the ASZ; and almost everywhere in the SIZ.

In the STZ, the variability of BGC-Argo properties is larger in the west region. The variability in the SAZ shows hot spots in the west region in both salinity, oxygen, nitrate, and pH, in the downstream region around  $\sim 70^\circ\text{E}$  (salinity, temperature, oxygen, and nitrate) and around  $100\text{--}110^\circ\text{E}$ . We find hot spots of variability in the PFZ between  $\sim 55\text{--}100^\circ\text{E}$  (upstream to downstream),  $\sim 110^\circ\text{E}$  (downstream, only for temperature), and around  $140\text{--}160^\circ\text{E}$  (east, for temperature and pH). There are several hot spots of larger variance for the ASZ profiles, which vary across the properties: The BGC-Argo variance is larger around  $20^\circ\text{E}$  (west region) for temperature and oxygen, around  $60^\circ\text{E}$  (upstream) for nitrate and pH, and around  $80^\circ\text{E}$  (downstream) for each of the properties. Finally, the SIZ shows larger variability west of  $10^\circ\text{E}$  (west) for temperature, oxygen, nitrate, and pH and a hot spot in variance at approximately  $140^\circ\text{E}$  (upstream) for salinity, temperature, and oxygen.

The structure of the variability is complex and hot spots of temperature and salinity normalized variance do not necessarily correspond to the locations of highest variability in BGC properties. This may be due to (1) BGC processes (e.g., carbonate production/dissolution), which modify the concentration of oxygen and nitrate and the pH of the waters; (2) the differing gradients of each property between fronts; (3) and the reduced spatial coverage of BGC data in some locations.

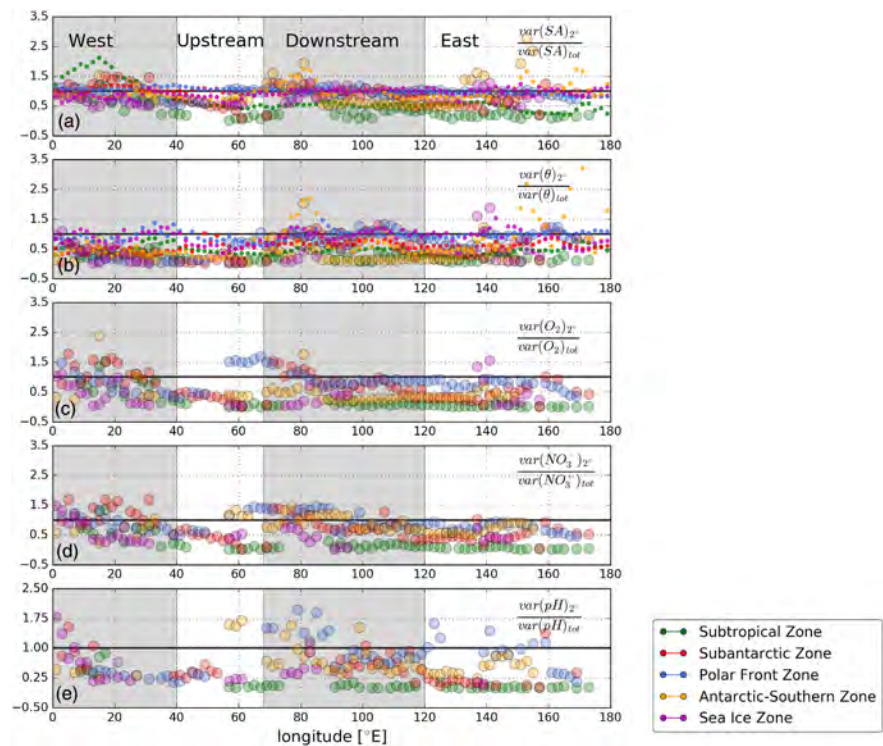


**Figure 16.** Regional variability of the ratio of binned ( $2^\circ$  in longitude) over the total variance of (a) absolute salinity (SA), (b) potential temperature ( $\theta$ ), (c) oxygen ( $O_2$ ), (d) nitrate ( $NO_3^-$ ), and (e) pH, along  $\Sigma_0$ , computed across the density classes around the Upper Circumpolar Deep Water. Markers are color coded as in Figure 14.

## 6. Discussion and Conclusions

The PCM approach (Maze, Mercier, & Cabanes, 2017) based on an unsupervised classification algorithm (here a Gaussian Mixture Model; Bilmes et al., 1998; Bishop, 2006) is applied to classify core Argo and BGC-Argo profiles into water mass regimes in the Indian sector of the Southern Ocean. To define SO frontal zones, the PCM method can be applied to vertical profiles of temperature and salinity between 300 and 900 m, below the portion of the water column most sensitive to air-sea exchange for most of the Argo profiles. We build upon recent studies that used temperature alone for the PCM (e.g., Jones et al., 2018; Maze, Mercier, Fablet, et al., 2017), and we included salinity in addition to temperature, measured by autonomous profiling floats, as this property is especially important in setting the stratification of the upper ocean in the subtropical and SIZs. The PCM identifies boundaries between the frontal zones, which are not continuous lines, but rather regions of sharp gradients (Chapman, 2017). In addition to automatically classifying each hydrographic profile into a unique frontal regime, this method allows us to use the posterior probability as a metric to highlight/identify possible regions of strong mixing and temporal variability (Figures 3 and 4). A region of larger mixing can be identified by lower probability (<70%, Figure 5). Mixing, such defined, is larger (1) at Southern Ocean fronts, (2) in the SAZ, and (3) in the major current systems of the STZ (cf. Figure 5 with Figure 9). Due to flow-topography interaction, these areas are hot spots of eddy kinetic energy (see Figure 5 in Llort et al., 2018 and Figure 3 in Roach et al., 2018), which can sustain intense events of vertical property exchange (Llort et al., 2018; Rosso et al., 2014), both within the AAIW density class (between the STF and PF) and within the UCDW (south of PF).

In this study, we find that the variability of the intermediate and deep waters is enhanced at topographic features (e.g., Crozet Plateau and KP) and in strong currents (e.g., at the subtropical Agulhas rings and Agulhas Return Current) but that the degree of variability differs for individual properties. AAIW temperature and salinity in the west region of the STZ are lowest west of  $40^\circ E$ , where colder, fresher, and oxygen-rich waters from the AAIW sourced in the Atlantic sector (west) and from the SAZ are mixed with the warmer, more saline, and oxygen-poorer Indian subtropical waters (east; Figure 12) (e.g., Talley, 1996). In the SAZ, AAIW mixes with the colder and fresher surface waters from the PFZ at KP, as evident by the minimum  $\theta$  of  $2^\circ C$

and SA of 34.25 in the downstream region (Figure 12). This mechanism is likely associated with cross-frontal intrusions, as suggested by Park et al. (1993), Park and Gamberoni (1997), and Sloyan and Rintoul (2001), where the convergence of fronts and highly energetic eddies can facilitate this injection of different waters and the subsequent modification of water masses (Park et al., 1993). Upon traversing KP, the averaged SAZ AAIW temperature and salinity increase again, while the oxygen concentration decreases, suggesting mixing with subtropical waters. Below the AAIW, the variation in the properties of the UCDW is marked not only by a strong meridional gradient across the different regimes but also by a large transition in the properties from west to east, where KP acts to homogenize the water mass (Figure 14). Hot spots of larger PV variability (Figure 15) suggest that the large change in each property is due not only to along isopycnal stirring but also diabatic transformations, as expected from the stronger vertical mixing that Whalen et al. (2012, 2015) show in these locations.

Argo has enabled us to study temperature, salinity, and, in some cases, oxygen properties across the vast Southern Ocean. Here, we demonstrate how the complementary array of BGC-Argo floats enables the assessment of the spatial variability of BGC properties. As physical and BGC states are influenced by diverse dynamics and gradients, we cannot fully infer where BGC properties might show larger variability by looking at only temperature and salinity variability. Given the rapidly increasing amount of Argo data (both core and BGC) and model output, the PCM method used here can serve as an important tool in future studies aiming to identify similarities in dynamical regimes (e.g., Ardyna et al., 2017; Jones et al., 2018; Liang et al., 2018; Maze, Mercier, Fablet, et al., 2017) and to reveal regions of strong mixing. Furthermore, BGC-Argo floats, strategically planned to target this KP region (Talley et al., 2019), can provide great insight regarding the distribution and the modification of water mass properties, highlighting the importance of targeting mixing hot spots in future observing arrays. Future work should explore these statistical methods to assess property changes and water mass evolution (e.g., in UCDW upwelling and its contribution to air-sea fluxes of carbon, oxygen, and heat) over the entire Southern Ocean.

Finally, we have only qualitatively compared our classification to fronts defined by Orsi et al. (1995). Future work should focus on a quantitative comparison of PCM determined fronts with fronts defined based on hydrography (e.g., Orsi et al., 1995), gradients of sea surface height (Sokolov & Rintoul, 2009b), or the new method by Chapman (2017) applied to absolute dynamic topography. Furthermore, the scientific community would benefit from a thorough comparison of our methodology with other existing novel algorithms, especially those methods that do not rely on a fixed number of clusters, such as the variational Bayesian GMM (Ghahramani & Beal, 2000).

#### Acknowledgments

SOCOM data were collected and made freely available by the Southern Ocean Carbon and Climate Observations and Modeling Project funded by the National Science Foundation, Division of Polar Programs (NSF PLR-1425989), supplemented by NASA, and by the International Argo Program and the NOAA programs that contribute to it. (<http://www.argo.ucsd.edu>, <http://argo.jcommops.org>). Argo data were collected and made freely available by the International Argo Program and the national programs that contribute to it. The Argo Program is part of the Global Ocean Observing System. I. R. thanks L. Böhme (University of St. Andrews), J. Bowman (Scripps Institution of Oceanography), Y. Liang (Woods Hole Oceanographic Institution), and M. Kuusela (Carnegie Mellon University) for all the valuable discussions on fronts and classification methods. This work is a contribution of the Southern Ocean Carbon and Climate Observations and Modeling project (SOCOM). SOCOM is supported by the National Science Foundation under NSF Award PLR-1425989. G. M. was supported by the French national programme LEFE/INSU, project SOMOVAR. We thank the anonymous reviewers who helped to improve this manuscript.

#### References

- Amante, C., & Eakins, B. W. (2009). ETOPO1 1 arc-minute global relief model: Procedures, data sources and analysis. US Department of Commerce, National Oceanic and Atmospheric Administration, National Environmental Satellite, Data and Information Service National Geophysical Data Center, Marine Geology and Geophysics Division Colorado.
- Aoki, S., Fujii, N., Ushio, S., Yoshikawa, Y., Watanabe, S., Mizuta, G., et al. (2008). Deep western boundary current and southern frontal systems of the Antarctic Circumpolar Current southeast of the Kerguelen Plateau. *Journal of Geophysical Research*, *113*, C08038. <https://doi.org/10.1029/2007JC004627>
- Aoki, S., Hariyama, M., Mitsudera, H., Sasaki, H., & Sasai, Y. (2007). Formation regions of Subantarctic Mode Water detected by OFES and Argo profiling floats. *Geophysical Research Letters*, *34*, L10606. <https://doi.org/10.1029/2007GL029828>
- Ardyna, M., Claustre, H., Sallée, J.-B., D'Ovidio, F., Gentili, B., Van Dijken, G., et al. (2017). Delineating environmental control of phytoplankton biomass and phenology in the Southern Ocean. *Geophysical Research Letters*, *44*, 5016–5024. <https://doi.org/10.1002/2016GL072428>
- Argo Data Management Team (2017). Argo user's manual v3.2. <https://doi.org/10.13155/29825>
- Argo Data Management Team (2018). Argo float data and metadata from Global Data Assembly Centre (Argo GDAC)—Snapshot of Argo GDAC of September 8st 2018. <https://doi.org/10.17882/42182>
- Bilmes, J. A. (1998). A gentle tutorial of the EM algorithm and its application to parameter estimation for Gaussian mixture and hidden Markov models. *International Computer Science Institute*, *4*(510), 126.
- Bishop, C. M. (2006). *Pattern recognition and machine learning*. New York: Springer.
- Briggs, E. M., Martz, T. R., Talley, L. D., Mazloff, M. R., & Johnson, K. S. (2018). Physical and biological drivers of biogeochemical tracers within the seasonal sea ice zone of the Southern Ocean from profiling floats. *Journal of Geophysical Research: Oceans*, *123*, 746–758. <https://doi.org/10.1002/2017JC012846>
- Cerovečki, I., & Mazloff, M. R. (2016). The spatiotemporal structure of diabatic processes governing the evolution of Subantarctic Mode Water in the Southern Ocean. *Journal of Physical Oceanography*, *46*(2), 683–710.
- Chapman, C. C. (2017). New perspectives on frontal variability in the Southern Ocean. *Journal of Physical Oceanography*, *47*(5), 1151–1168.
- Donohue, K. A., Hufford, G. E., & McCartney, M. S. (1999). Sources and transport of the deep western boundary current east of the Kerguelen Plateau. *Geophysical Research Letters*, *26*(7), 851–854.
- Freeman, N. M., & Lovenduski, N. S. (2016). Mapping the Antarctic Polar Front: Weekly realizations from 2002 to 2014. *Earth System Science Data*, *8*(1), 191–198.

- Freeman, N. M., Lovenduski, N. S., & Gent, P. R. (2016). Temporal variability in the Antarctic Polar Front (2002–2014). *Journal of Geophysical Research: Oceans*, *121*, 7263–7276. <https://doi.org/10.1029/96JC00203>
- Freeman, N. M., Munro, D. R., Sprintall, J., Mazloff, M. R., Purkey, S., Rosso, I., et al. (2019). The observed seasonal cycle of macronutrients in Drake Passage: Relationship to fronts and utility as a model metric. *Journal of Geophysical Research: Oceans*, *124*, 4763–4783. <https://doi.org/10.1029/2019JC015052>
- Fukamachi, Y., Rintoul, S., Church, J., Aoki, S., Sokolov, S., Rosenberg, M., & Wakatsuchi, M. (2010). Strong export of Antarctic Bottom Water east of the Kerguelen Plateau. *Nature Geoscience*, *3*(5), 327.
- Ghahramani, Z., & Beal, M. J. J. (2000). Variational inference for Bayesian mixtures of factor analysers. In *Advances in neural information processing systems* (Vol. 12, No. 12, pp. 449–455). Cambridge, MA: MIT Press.
- Gray, A. R., Johnson, K. S., Bushinsky, S. M., Riser, S. C., Russell, J. L., Talley, L. D., et al. (2018). Autonomous biogeochemical floats detect significant carbon dioxide outgassing in the high-latitude Southern Ocean. *Geophysical Research Letters*, *45*, 9049–9057. <https://doi.org/10.1029/2018GL078013>
- Gruber, N., Gloor, M., Mikaloff Fletcher, S. E., Doney, S. C., Dutkiewicz, S., Follows, M. J., et al. (2009). Oceanic sources, sinks, and transport of atmospheric CO<sub>2</sub>. *Global Biogeochemical Cycles*, *23*, GB1005. <https://doi.org/10.1029/2008GB003349>
- Hanawa, K., & Talley, L. D. (2001). Mode waters. Ocean circulation and climate. In G. Siedler et al. (Eds.), *International Geophysics Series* (pp. 373–386).
- Hartigan, J. A., & Wong, M. A. (1979). Algorithm AS 136: A k-means clustering algorithm. *Journal of the Royal Statistical Society. Series C (Applied Statistics)*, *28*(1), 100–108.
- IOC, SCOR, & IAPSO (2010). The international thermodynamic equation of seawater–2010: Calculation and use of thermodynamic properties.[includes corrections up to 31st october, 2015].
- Ito, T., Woloszyn, M., & Mazloff, M. (2010). Anthropogenic carbon dioxide transport in the Southern Ocean driven by Ekman flow. *Nature*, *463*(7277), 80–83.
- Johnson, K. S., Plant, J. N., Coletti, L. J., Jannasch, H. W., Sakamoto, C. M., Riser, S. C., et al. (2017). Biogeochemical sensor performance in the SOCCOM profiling float array. *Journal of Geophysical Research: Oceans*, *122*, 6416–6436. <https://doi.org/10.1002/2017JC012838>
- Johnson, K. S., Riser, S. C., Boss, E. S., Talley, L. D., Sarmiento, J. L., Swift, D. D., et al. (2018). SOCCOM float data—Snapshot 2018-09-12. In Southern Ocean Carbon and Climate Observations and Modeling (SOCCOM) Float Data Archive. <https://doi.org/10.6075/J0QJ7FJP>
- Jones, D. C., Holt, H. J., Meijers, A. J., & Shuckburgh, E. F. (2018). Unsupervised clustering of Southern Ocean Argo float temperature profiles. *Journal of Geophysical Research: Oceans*, *124*, 390–402. <https://doi.org/10.1029/2018JC014629>
- Konishi, S., & Kitagawa, G. (2008). *Bayesian information criteria* (pp. 211–237). New York, NY: Springer New York.
- Liang, Y.-C., Mazloff, M. R., Rosso, I., Fang, S.-W., & Yu, J.-Y. (2018). A multivariate empirical orthogonal function method to construct nitrate maps in the Southern Ocean. *Journal of Atmospheric and Oceanic Technology*, *35*(7), 1505–1519.
- Llort, J., Langlais, C., Matear, R., Moreau, S., Lenton, A., & Strutton, P. G. (2018). Evaluating Southern Ocean carbon eddy-pump from biogeochemical-Argo Floats. *Journal of Geophysical Research: Oceans*, *123*, 971–984. <https://doi.org/10.1002/2017JC012861>
- Maraldi, C., Mongin, M., Coleman, R., & Testut, L. (2009). The influence of lateral mixing on a phytoplankton bloom: Distribution in the Kerguelen Plateau region. *Deep Sea Research Part I*, *56*, 963–973.
- Maze, G., Mercier, H., & Cabanes, C. (2017). Profile Classification Models. *Mercator Ocean Journal*, *55*, 48–56.
- Maze, G., Mercier, H., Fablet, R., Tandeo, P., Radenco, M. L., Lenca, P., et al. (2017). Coherent heat patterns revealed by unsupervised classification of Argo temperature profiles in the North Atlantic Ocean. *Progress in Oceanography*, *151*, 275–292.
- McCarthy, M. C., & Talley, L. D. (1999). Three-dimensional isoneutral potential vorticity structure in the Indian Ocean. *Journal of Geophysical Research*, *104*(C6), 13,251–13,267.
- McCartney, M. (1977). Subantarctic Mode Water. A voyage of discovery, George Deacon 70th Anniversary Volume. pp. 103–119.
- McCartney, M. S., & Donohue, K. A. (2007). A deep cyclonic gyre in the Australian–Antarctic Basin. *Progress in Oceanography*, *75*(4), 675–750. <https://doi.org/10.1016/j.pocean.2007.02.008>
- Meyer, A., Sloyan, B. M., Polzin, K. L., Phillips, H. E., & Bindoff, N. L. (2015). Mixing variability in the Southern Ocean. *Journal of Physical Oceanography*, *45*(4), 966–987.
- Moore, J. K., Abbott, M. R., & Richman, J. G. (1997). Variability in the location of the Antarctic Polar Front (90–20°W) from satellite sea surface temperature data. *Journal of Geophysical Research*, *102*(C13), 27,825–27,833.
- Orsi, A. H., Whitworth, T. III, & Nowlin, W. D. Jr (1995). On the meridional extent and fronts of the Antarctic Circumpolar Current. *Deep Sea Res. Part I: Oceanographic Research Papers*, *42*(5), 641–673.
- Park, Y.-H., Durand, I., Kestenare, E., Rougier, G., Zhou, M., d'Ovidio, F., et al. (2014). Polar Front around the Kerguelen Islands: An up-to-date determination and associated circulation of surface/subsurface waters. *Journal of Geophysical Research: Oceans*, *119*, 6575–6592. <https://doi.org/10.1002/2014JC010061>
- Park, Y.-H., Fuda, J.-L., Durand, I., & Naveira Garabato, A. C. (2008). Internal tides and vertical mixing over the Kerguelen Plateau. *Deep Sea Research Part II*, *55*(5–7), 582–593.
- Park, Y.-H., & Gamberoni, L. (1997). Cross-frontal exchange of Antarctic Intermediate Water and Antarctic Bottom Water in the Crozet Basin. *Deep Sea Research Part II: Topical Studies in Oceanography*, *44*(5), 963–986.
- Park, Y.-H., Gamberoni, L., & Charriaud, E. (1993). Frontal structure, water masses, and circulation in the Crozet Basin. *Journal of Geophysical Research*, *98*(C7), 12,361–12,385.
- Park, Y.-H., Roquet, F., Durand, I., & Fuda, J.-L. (2008). Large-scale circulation over and around the Northern Kerguelen Plateau. *Deep Sea Research Part II*, *55*, 566–581.
- Park, Y.-H., Vivier, F., Roquet, F., & Kestenare, E. (2009). Direct observations of the ACC transport across the Kerguelen Plateau. *Geophysical Research Letters*, *36*, L18603. <https://doi.org/10.1029/2009GL039617>
- Pedregosa, F., Varoquaux, G., Gramfort, A., Michel, V., Thirion, B., Grisel, O., et al. (2011). Scikit-learn: Machine learning in Python. *Journal of Machine Learning Research*, *12*, 2825–2830.
- Piola, A. R., & Georgi, D. T. (1982). Circumpolar properties of Antarctic intermediate water and Subantarctic Mode Water, Deep Sea Research Part A. *Oceanographic Research Papers*, *29*(6), 687–711.
- Piola, A. R., & Gordon, A. L. (1989). Intermediate waters in the southwest South Atlantic. *Deep Sea Research Part A. Oceanographic Research Papers*, *36*(1), 1–16.
- Prézelin, B. B., Hofmann, E. E., Mengelt, C., & Klinck, J. M. (2000). The linkage between Upper Circumpolar Deep Water (UCDW) and phytoplankton assemblages on the west Antarctic Peninsula continental shelf. *Journal of Marine Research*, *58*(2), 165–202.
- Read, J., & Pollard, R. (1993). Structure and transport of the Antarctic Circumpolar Current and Agulhas Return Current at 40°E. *Journal of Geophysical Research*, *98*(C7), 12,281–12,295.

- Riser, S. C., Swift, D., & Drucker, R. (2018). Profiling floats in SOCCOM: Technical capabilities for studying the Southern Ocean. *Journal of Geophysical Research: Oceans*, *123*, 4055–4073. <https://doi.org/10.1002/2017JC013419>
- Roach, C. J., Balwada, D., & Speer, K. (2018). Global observations of horizontal mixing from Argo float and surface drifter trajectories. *Journal of Geophysical Research: Oceans*, *123*, 4560–4575. <https://doi.org/10.1029/2018JC013750>
- Roquet, F., Park, Y.-H., Guinet, C., Bailleul, F., & Charrassin, J.-B. (2009). Observations of the Fawn Trough Current over the Kerguelen Plateau from instrumented elephant seals. *Journal of Marine Systems*, *78*(3), 377–393.
- Rosso, I., Hogg, A. M., Matear, R., & Strutton, P. G. (2016). Quantifying the influence of sub-mesoscale dynamics on the supply of iron to Southern Ocean phytoplankton blooms. *Deep Sea Research Part I: Oceanographic Research Papers*, *115*, 199–209.
- Rosso, I., Hogg, M. A., Strutton, G. P., Kiss, E. A., Matear, R., Klocker, A., & van Sebille, E. (2014). Vertical transport in the ocean due to sub-mesoscale structures: Impacts in the Kerguelen region. *Ocean Modelling*, *80*, 10–23.
- Rosso, I., Mazloff, M. R., Verdy, A., & Talley, L. D. (2017). Space and time variability of the Southern Ocean carbon budget. *Journal of Geophysical Research: Oceans*, *122*, 7407–7432. <https://doi.org/10.1002/2016JC012646>
- Sabine, C. L., Feely, R. A., Johnson, G. C., Strutton, P. G., Lamb, M. F., & McTaggart, K. E. (2004). A mixed layer carbon budget for the GasEx-2001 experiment. *Journal of Geophysical Research*, *109*, C08S05. <https://doi.org/10.1029/2002JC001747>
- Sallée, J.-B., Speer, K., & Rintoul, S. (2011). Mean-flow and topographic control on surface eddy-mixing in the Southern Ocean. *Journal of Marine Research*, *69*(4–5), 753–777. <https://doi.org/10.1357/002224011799849408>
- Sallée, J.-B., Speer, K., Rintoul, S., & Wijffels, S. (2010). Southern Ocean thermocline ventilation. *Journal of Physical Oceanography*, *40*(3), 509–529.
- Sallée, J.-B., Wienders, N., Speer, K., & Morrow, R. (2006). Formation of Subantarctic Mode Water in the southeastern Indian Ocean. *Ocean Dynamics*, *56*(5–6), 525–542.
- Sarmiento, J. á., Gruber, N., Brzezinski, M., & Dunne, J. (2004). High-latitude controls of thermocline nutrients and low latitude biological productivity. *Nature*, *427*(6969), 56.
- Schwarz, G., et al. (1978). Estimating the dimension of a model. *The annals of statistics*, *6*(2), 461–464.
- Sloyan, B. M., & Rintoul, S. R. (2001). Circulation, renewal, and modification of Antarctic Mode and Intermediate Water. *Journal of Physical Oceanography*, *31*(4), 1005–1030.
- Sloyan, B. M., Talley, L. D., Chereskin, T. K., Fine, R., & Holte, J. (2010). Antarctic Intermediate Water and Subantarctic Mode Water formation in the southeast Pacific: The role of turbulent mixing. *Journal of Physical Oceanography*, *40*(7), 1558–1574.
- Sokolov, S., & Rintoul, S. R. (2009a). Circumpolar structure and distribution of the Antarctic Circumpolar Current fronts: 2. Variability and relationship to sea surface height. *Journal of Geophysical Research*, *114*, C11019. <https://doi.org/10.1029/2008JC005248>
- Sokolov, S., & Rintoul, S. R. (2009b). Circumpolar structure and distribution of the Antarctic Circumpolar Current fronts: 1. Mean circumpolar paths. *Journal of Geophysical Research*, *114*, C11018. <https://doi.org/10.1029/2008JC005108>
- Sparrow, M. D., Heywood, K. J., Brown, J., & Stevens, D. P. (1996). Current structure of the South Indian Ocean. *Journal of Geophysical Research*, *101*(C3), 6377–6391.
- Takahashi, T., Sutherland, S. C., Wanninkhof, R., Sweeney, C., Feely, R. A., Chipman, D. W., et al. (2009). Climatological mean and decadal change in surface ocean pCO<sub>2</sub>, and net sea-air CO<sub>2</sub> flux over the global oceans. *Deep Sea Research Part II: Topical Studies in Oceanography*, *56*(8), 554–577.
- Talley, L. (1996). Antarctic Intermediate Water in the South Atlantic. In *The South Atlantic* (pp. 219–238). Berlin, Heidelberg: Springer.
- Talley, L. D. (2013). Closure of the global overturning circulation through the Indian, Pacific, and Southern Oceans: Schematics and transports. *Oceanography*, *26*(1), 80–97.
- Talley, L. D., Pickard, G. L., Emery, W. J., & Swift, J. H. (2011). *Descriptive physical oceanography: An introduction* (6 ed., 560 pp). Boston: Elsevier.
- Talley, L., Rosso, I., Kamenkovich, I., Mazloff, M., Wang, J., Boss, E., et al. (2019). Southern Ocean biogeochemical float deployment strategy with example from the Greenwich Meridian line (GO-SHIP A12), *124*, 403–431. <https://doi.org/10.1029/2018JC014059>
- Tamsitt, V., Drake, H. F., Morrison, A. K., Talley, L. D., Dufour, C. O., Gray, A. R., et al. (2017). Spiraling pathways of global deep waters to the surface of the Southern Ocean. *Nature Communications*, *8*(1), 172.
- Tamsitt, V., Talley, L. D., Mazloff, M. R., & Cerovečki, I. (2016). Zonal variations in the Southern Ocean heat budget. *Journal of Climate*, *29*(18), 6563–6579.
- Van Beek, P., Bourquin, M., Reyss, J.-L., Souhaut, M., Charette, M., & Jeandel, C. (2008). Radium isotopes to investigate the water mass pathways on the Kerguelen Plateau (Southern Ocean). *Deep Sea Research Part II*, *55*(5), 622–637.
- Whalen, C. B., MacKinnon, J. A., Talley, L. D., & Waterhouse, A. F. (2015). Estimating the mean diapycnal mixing using a finescale strain parameterization. *Journal of Physical Oceanography*, *45*(4), 1174–1188.
- Whalen, C., Talley, L., & MacKinnon, J. (2012). Spatial and temporal variability of global ocean mixing inferred from Argo profiles. *Geophysical Research Letters*, *39*, L18612. <https://doi.org/10.1029/2012GL053196>
- Williams, N., Juranek, L., Feely, R., Russell, J., Johnson, K., & Hales, B. (2018). Assessment of the carbonate chemistry seasonal cycles in the Southern Ocean from persistent observational platforms. *Journal of Geophysical Research: Oceans*, *123*, 4833–4852. <https://doi.org/10.1029/2017JC012917>
- Wong, A., Keeley, R., Carval, T., & Argo Data Management Team (2012). Argo quality control manual Version 2.7.